


Extended magic phase in twisted graphene multilayers

D. C. W. Foo^{1,*}, Z. Zhan^{2,†}, Mohammed M. Al Ezzi^{1,3}, L. Peng³, S. Adam^{1,3,4,5} and F. Guinea^{2,6}¹Centre for Advanced 2D Materials, National University of Singapore, Singapore 117546²IMDEA Nanociencia, 28049 Madrid, Spain³Department of Physics, Faculty of Science, National University of Singapore, Singapore 117542⁴Department of Materials Science and Engineering, National University of Singapore, Singapore 117575⁵Yale-NUS College, Singapore 138527⁶Donostia International Physics Center, 20018 San Sebastián, Spain (Received 29 May 2023; revised 4 January 2024; accepted 8 January 2024; published 13 February 2024)

Theoretical and experimental studies have verified the existence of “magic angles” in twisted bilayer graphene, where the rotation angle between layers gives rise to flat bands and consequently exotic correlated phases. Recently, magic-angle phenomena have been predicted and reported in other graphene systems, for instance, multilayers with alternating twist angles and trilayers with identical twist angles between consecutive layers. In this paper, we present a comprehensive theoretical study on flat bands in general twisted graphene systems. Using the continuum model in the chiral limit, we demonstrate the existence of flat bands in a variety of multilayers where the ratios between twist angles are rational and develop a framework for predicting magic-angle sets in trilayer configurations with arbitrary ratio of rotation angles. Our results are corroborated by tight-binding calculations. Remarkably, the technique we developed can be extended to systems with many layers of graphene. Our results suggest that flat bands can exist in graphene multilayers with angle disorder, that is, narrow samples of turbostatic graphite, point to the existence of a continuous, connected magic surface in trilayer configuration space, and compare favourably with contemporary experiments on trilayer moiré quasicrystals.

DOI: [10.1103/PhysRevResearch.6.013165](https://doi.org/10.1103/PhysRevResearch.6.013165)

I. INTRODUCTION

Twisted bilayer graphene (tBG) has proven to be a fertile platform for condensed-matter physics studies owing to the remarkable tunability of the Fermi velocity and electronic structure through the twist angle [1]. In particular, at the “magic angles” [2] in tBG, $\theta_{\text{tBG}}^M \approx 1.1^\circ$, the Fermi velocity vanishes, allowing for strongly correlated phases where interactions dominate over the kinetic energy [3,4].

This has led to a resurgence of interest in moiré systems, including but not limited to Van der Waals heterostructures [5–8], transition metal dichalcogenides [9–12], and graphene multilayers [13–16]. One particularly successful avenue of investigation has been the extension of the arguments demonstrating the existence of magic angles in tBG [17,18] to graphene multilayers [19], which found simple geometric relations between the bilayer and multilayer magic angles, predictions that were later verified experimentally [20–22]. Later, numerical studies have built on these foundations, demonstrating for example that the existence of flat bands is

robust against perpendicular magnetic fields [23] and asymmetry of the layer parameters [24], and that peaks in the density of states (DOS) appear, and are resistant to relaxation [25], for trilayer configurations beyond the canonical alternating-twist case [26]. Recent work has predicted magic angles in the equal twist trilayer graphene case [27], and a magic line, with magic angles as a function of pressure, in twisted WSe₂ [28], suggesting that similar extended magic surfaces may exist in the generalized configuration space of graphene multilayers. Previous work has typically had a limited focus on specific, highly symmetric trilayer arrangements [19,27] or else has confined exploration to particular slices of configuration space that were already known to contain magic angles [26]. In this work we demonstrate the existence of flat bands in multilayers with generic, commensurate twist angles and provide an approximate analytic continuation to the incommensurate case, indicating an extended $N - 2$ -dimensional magic surface in the space of $N - 1$ twist angles characterizing N layers, with particular emphasis on generic twisted trilayer graphene (tTG).

A prior study [19] noted that in the particular case of unshifted, alternating twist graphene multilayers, the Hamiltonian may be exactly decomposed into a direct sum of bilayer graphene Hamiltonians (with an additional monolayer for odd number of layers), with the moiré potential identical up to a scalar multiple. This allows one to directly read off the magic angles of multilayer stacks. In contrast, other trilayer configurations have more complex effective moiré potentials, though magic angle physics may still be possible [29]. In

*c2ddf@nus.edu.sg

†zhzhanh@gmail.com

Published by the American Physical Society under the terms of the [Creative Commons Attribution 4.0 International](https://creativecommons.org/licenses/by/4.0/) license. Further distribution of this work must maintain attribution to the author(s) and the published article's title, journal citation, and DOI.

particular, a strongly correlated superconducting state has been observed in a trilayer system with incommensurate twist angles [30].

We note also for completeness related work in the general field of double moiré systems, particularly that of tBG on hexagonal boron nitride (hBN) which indicates narrow bands may persist with the presence of a substrate [31–33], and of hBN encapsulated graphene [34], where the two similar but incommensurate moiré potentials lead to fractal structure in the band gaps. Nevertheless, these may be sufficiently distinguished from the present study in the first instance as they were not primarily concerned with finding flat bands and magic angles at all, and in the second due to key differences between graphene and hBN. For example, the low-energy physics of these systems are typically dominated by the graphene layers and associated wave functions, with the hBN only serving as an intermediary [35]. Correspondingly, no nonmonotonic behavior of Fermi velocity or bandwidth is expected in monolayer graphene/hBN systems [36], while nonmonotonic, that is, magic physics is the hallmark of graphene multilayers.

II. MOIRÉ LATTICES IN TWISTED GRAPHENE TRILAYERS AND IN OTHER TWISTED STACKS

The electronic structure of a twisted bilayer can be reasonably approximated by a periodic moiré structure [1,2], irrespective of whether the two layers are commensurate at the atomic scale. The situation is more complex in twisted stacks with more than two layers [26,37–43]. In a trilayer, for instance, two twist angles between nearest-neighbor layers can be defined, θ_{12} and θ_{23} , shown in Fig. 1(a). Except for the case mentioned above of multilayers where the twist angle is of equal magnitude and opposite sign between nearest-neighbor pairs of layers [19], no simple global moiré structure can be defined.

An approximate moiré lattice can be defined if the relative angle between the Brillouin zones defined by the twist angles between different pairs of layers is neglected [39,41,42]. For instance, in a trilayer with two different twist angles, θ_{12} , θ_{23} , this approximation becomes exact when $\theta_{12} = \theta_{23}$ in the limit $\theta_{12} \rightarrow 0$, although corrections [43] are required for physically relevant angles, $\theta_{12}, \theta_{23} \approx 1^\circ$. It is worth noting that this approximation, for a trilayer, has a dependence not only on the angles θ_{12}, θ_{23} but also on the relative displacement of the moiré potentials, \mathbf{D} illustrated in Fig. 1(b) [40]. The dependence is periodic on \mathbf{D} , with wavelength of the order of the moiré length scales.

It can be shown [44] that the approximation mentioned above defined by a moiré lattice commensurate with the two twist angles and a displacement between the top and bottom layers describes *locally* the full problem of the trilayer. For the case of approximately commensurate twist angles, $\theta_{12} \approx m\theta_0$, $\theta_{23} \approx n\theta_0$, where m, n are coprime integers, the interlayer tunneling terms in the trilayer continuum Hamiltonian can be written as containing two periodicities: (i) the periodicity, ℓ_m , of the moiré problem obtained by neglecting the angle between the two Brillouin zones defined by θ_{12}, θ_{23} , of order d/θ_0 , where d is the lattice constant of graphene, and (ii) a periodicity, ℓ_{m_2} obtained by modulating

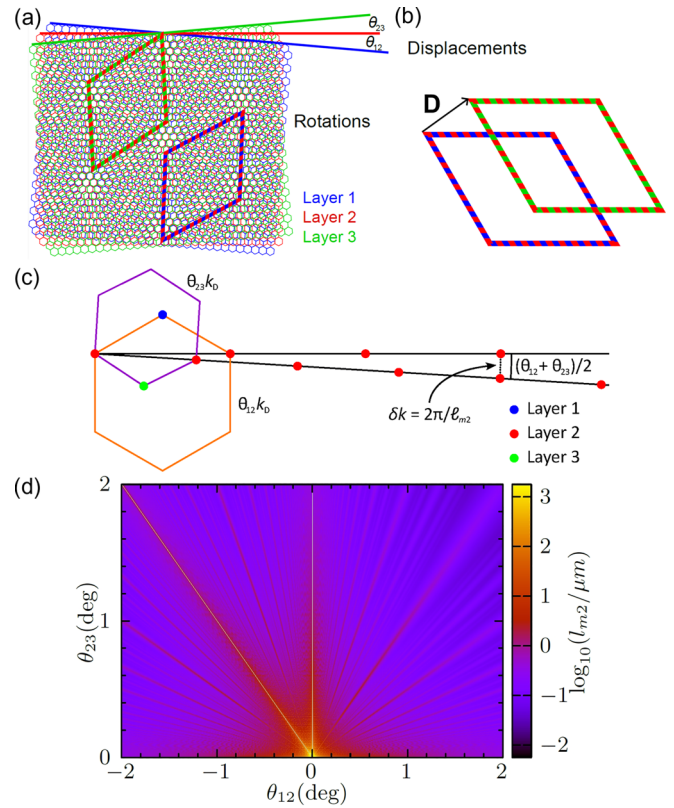


FIG. 1. Moiré-of-moiré periodicity. Schematic illustrating the trilayer parameters (a) twist angle pairs and (b) the moiré displacement \mathbf{D} . The moiré unit cell of tBG with θ_{12} is outlined by a rhombus with alternating colors red and blue and θ_{23} with colors red and green. The rhombus vertices lie at AA stacking regions of the respective layers. (c) Sketch of connected momentum states between layers with misaligned moiré patterns (orange and purple), resulting in a moiré-of-moiré modulation. Large angles $\theta_{12} = 4^\circ$, $\theta_{23} = 3^\circ$ are used for clarity, and less misalignment is expected for real magic-angle samples. The length scale of this modulation is determined by the closest approach of second layer lattice sites formed from the two moiré patterns, indicated with a dotted line. The local expansion used in numerical calculation neglects this misalignment and, for commensurate angles, collapses this distance to zero. (d) Log-scale plot of the moiré-of-moiré length scale, l_{m_2} , in microns, as a function of twist angles. The left diagonal in white marks the line $\theta_{12} = -\theta_{23}$, where there is no misalignment and l_{m_2} diverges. l_{m_2} also diverges when either angle is zero and there is no moiré-of-moiré pattern to speak of.

the displacement \mathbf{D} , over a larger unit cell whose dimensions scale as d/θ_0^2 . Each tBG pair in tTG defines a momentum-space moiré unit cell, purple and orange in Fig. 1(c), whose misalignment leads to misalignment of the moiré lattices, shown with the black lines and the finite δk . Neglecting this moiré misalignment forces the black lines to coincide, and for commensurate angles forces $\delta k = 0$. δk therefore is conjugate to ℓ_{m_2} . For small values of θ_0 , shown in Fig. 1(d), this scaling behavior implies that $\ell_m \ll \ell_{m_2}$, as ℓ_{m_2} can reach values of microns for $\theta_0 \lesssim 1^\circ$. Further details may be found in Appendix C.

It is worth noting that small and layer-dependent biaxial strains can exactly align the Brillouin zones associated to

different twist angles, θ_{12}, θ_{23} , so that $\ell_{m2} \rightarrow \infty$ and the approximation which makes use of a single moiré lattice defined by ℓ_m becomes exact, see Ref. [45]. These strains imply a small relaxation of the lattice [45]. This analysis has been extended to some commensurate cases of trilayers with unequal twist angles [46].

III. CHIRALLY SYMMETRIC CONTINUUM MODEL AND NECESSITY OF NUMERICAL COMPUTATION

We use a chirally symmetric version of the Bistritzer-Macdonald continuum model [2] that is exactly computable for commensurate angle pairs $(\theta_{12}, \theta_{23})$ and approximately solvable for incommensurate angle pairs. These results will later be supplemented by calculations on a tight-binding model [26] that we extend to deal with general angle and layer displacement. See Appendix D for details of the tight-binding model.

We begin with the tBG Hamiltonian

$$\mathcal{H}_{\text{tBG}} = \begin{bmatrix} 0 & \mathcal{D}_2^\dagger(\mathbf{r}, \alpha) \\ \mathcal{D}_2(\mathbf{r}, \alpha) & 0 \end{bmatrix}_{\text{AB}}, \quad (1)$$

where the subscript AB indicates sublattice space and the zeros on the diagonals are the natural consequence of using the chirally symmetric model. The layer space submatrix is given by

$$\mathcal{D}_2(\mathbf{r}, \alpha) = \mathbb{1}_2 \bar{\delta} + \alpha \begin{bmatrix} 0 & U(\mathbf{r}) \\ U(-\mathbf{r}) & 0 \end{bmatrix}_L, \quad (2)$$

where $\bar{\delta} = -i(\partial_x + i\partial_y)$, $\mathbb{1}_2$ is the rank-2 identity matrix, $\alpha \equiv 4\pi v_F/dw(2 \sin \theta/2) \approx 4\pi v_F/dw\theta$ for v_F the Fermi velocity, d the graphene lattice constant, w the interlayer hopping, θ the twist angle and we take the small-angle approximation. $U(\mathbf{r}) = \sum_{j=1,2,3} e^{i\frac{2\pi(j-1)}{3}} e^{i\mathbf{g}_j \cdot \mathbf{r}}$ is the moiré potential with $\mathbf{g}_1 = \frac{4\pi\theta}{3d}(0, 1)$, $\mathbf{g}_j = R_{2\pi/3}^{j-1} \mathbf{g}_1$ the vectors connecting each moiré K point to the three nearest K' points, and R_ϕ rotates a vector by angle ϕ . The flat band equation is then $\mathcal{D}_2(\mathbf{r}, \alpha_2^{(n)})\psi^{(n)}(\mathbf{r}) = 0$ or, in terms of the explicit components, the set of equations

$$\bar{\delta}\psi_1^{(n)}(\mathbf{r}) + \alpha_2^{(n)}U(\mathbf{r})\psi_2^{(n)}(\mathbf{r}) = 0, \quad (3)$$

$$\alpha_2^{(n)}U(-\mathbf{r})\psi_1^{(n)}(\mathbf{r}) + \bar{\delta}\psi_2^{(n)}(\mathbf{r}) = 0, \quad (4)$$

and the solutions for $\psi^{(n)}(\mathbf{r})$ and $\alpha_2^{(n)}$ are known [18]. The chirally symmetric tTG Hamiltonian may similarly be expressed in the form

$$\mathcal{H}_{\text{tTG}} = \begin{bmatrix} 0 & \mathcal{D}_3^\dagger(\mathbf{r}, \mathbf{D}, \alpha, \eta) \\ \mathcal{D}_3(\mathbf{r}, \mathbf{D}, \alpha, \eta) & 0 \end{bmatrix}_{\text{AB}}, \quad (5)$$

where the three-layer submatrix is given by

$$\begin{aligned} & \mathcal{D}_3(\mathbf{r}, \mathbf{D}, \alpha, \eta) \\ &= \mathbb{1}_3 \bar{\delta} + \alpha \begin{bmatrix} 0 & U(\mathbf{r}) & 0 \\ U(-\mathbf{r}) & 0 & U(\eta(\mathbf{r} - \mathbf{D})) \\ 0 & U(-\eta(\mathbf{r} - \mathbf{D})) & 0 \end{bmatrix}_L, \end{aligned} \quad (6)$$

where α and the \mathbf{g}_j of U are now defined in terms of θ_{12} and $\eta \equiv \frac{\theta_{23}}{\theta_{12}}$ is the angle ratio. For now we neglect the

small rotation of the second moiré potential due to incommensurability of the twists, though accounting for this only strengthens the argument to come. The flat band equation is now $\mathcal{D}_3(\mathbf{r}, \mathbf{D}, \alpha_3^{(n)}, \eta)\Psi^{(n)}(\mathbf{r}) = 0$, which may be written explicitly in component form as

$$\bar{\delta}\Psi_1^{(n)}(\mathbf{r}) + \alpha_3^{(n)}U(\mathbf{r})\Psi_2^{(n)}(\mathbf{r}) = 0, \quad (7)$$

$$\begin{aligned} & \bar{\delta}\Psi_2^{(n)}(\mathbf{r}) + \alpha_3^{(n)}U(-\mathbf{r})\Psi_1^{(n)}(\mathbf{r}) + \alpha_3^{(n)}U(\eta(\mathbf{r} - \mathbf{D}))\Psi_3^{(n)}(\mathbf{r}) \\ &= 0, \end{aligned} \quad (8)$$

$$\bar{\delta}\Psi_3^{(n)}(\mathbf{r}) + \alpha_3^{(n)}U(-\eta(\mathbf{r} - \mathbf{D}))\Psi_2^{(n)}(\mathbf{r}) = 0. \quad (9)$$

If we wish to establish a connection to tBG in the manner of previous studies [19,27], then the only ingredients available to us with which to construct $\Psi^{(n)}$ are the components of the tBG flat band spinor, $\psi_1^{(n)}(\mathbf{r})$, $\psi_2^{(n)}(\mathbf{r})$, $\psi_1^{(n)}(\eta(\mathbf{r} - \mathbf{D}))$, and $\psi_2^{(n)}(\eta(\mathbf{r} - \mathbf{D}))$. We note here that the set of these functions, along with $U(\mathbf{r})$, $U(-\mathbf{r})$, $U(\eta(\mathbf{r} - \mathbf{D}))$, and $U(-\eta(\mathbf{r} - \mathbf{D}))$, is linearly independent unless both $|\eta| = 1$ and \mathbf{D} equal to either zero or a moiré lattice vector.

From Eq. (3) and Eq. (7), $\Psi_1^{(n)}$ can only contain terms involving $\psi_1^{(n)}(\mathbf{r})$, so $\Psi_2^{(n)}$ must contain terms involving $\psi_2^{(n)}(\mathbf{r})$ and must not contain terms involving either $\psi_1^{(n)}(\eta(\mathbf{r} - \mathbf{D}))$ or $\psi_2^{(n)}(\eta(\mathbf{r} - \mathbf{D}))$; similarly from Eq. (4) and Eq. (9), $\Psi_3^{(n)}$ can only contain terms involving $\psi_2^{(n)}(\eta(\mathbf{r} - \mathbf{D}))$, meaning $\Psi_2^{(n)}$ must contain terms involving $\psi_1^{(n)}(\eta(\mathbf{r} - \mathbf{D}))$ and must not contain terms involving either $\psi_1^{(n)}(\mathbf{r})$ or $\psi_2^{(n)}(\mathbf{r})$, contradicting the first statement. It is therefore not possible for solutions to the tTG flat band equation at general η , \mathbf{D} to be constructed solely from those of the tBG flat band solution, and there is therefore no correspondence between any existing magic angles for general η , \mathbf{D} , tTG and those of tBG. Furthermore, as the moiré potential matrix, the off-diagonal parts of \mathcal{D}_3 , is singular, one cannot find a unique solution for the perturbation to the n th magic angle in response to small η or \mathbf{D} as some linear function of the set of $|\eta| = 1$, zero displacement magic angles. In other words, the breakdown of the tBG-tTG correspondence is nonperturbative.

While this analysis makes clear the breakdown of correspondence between tBG and tTG magic angles, it does not mean that tTG magic angles do not exist, only that they cannot be predicted through some analytic function of the tBG magic angles.

An approximate solution may be considered, however, if one angle is much larger than the other. This is further divided into two distinct cases, $|\eta| \ll 1$, and $|\eta| \gg 1$. In the former case, $U(\eta(\mathbf{r} - \mathbf{D}))$ vanishes, the system tends to an uncoupled mono-bilayer, and the magic angle is given by the tBG magic angle. In the latter case, the low-energy fermions are unable to resolve the details of the rapidly oscillating $U(\eta(\mathbf{r} - \mathbf{D}))$, interacting only with its zero average. As a result, one layer effectively decouples, resulting once again in an uncoupled mono-bilayer system. It is therefore expected that the magic angle will tend to the tBG value, as seen in Figs. 2 and 3. Note that the former limit is in a regime where the theory breaks down, which can be seen in the case of tBG as the off-diagonal moiré potential does not tend to the interlayer hopping of Bernal stacked bilayer graphene in the untwisted

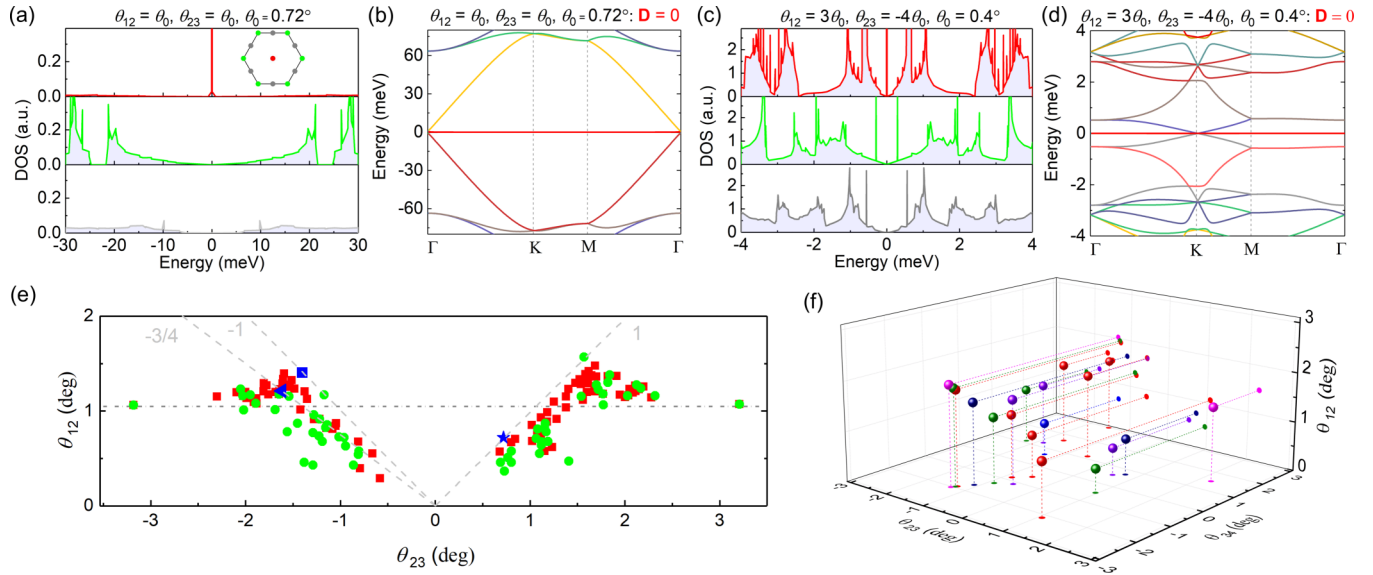


FIG. 2. Magic angles in the chiral limit. (a) Local DOS of a graphene trilayer in the chiral limit with $\theta_{12} = \theta_{23} = \theta_0 = 0.72^\circ$ (magic angle for zero displacement) for three different displacements \mathbf{D} between the top and bottom layers. The inset on the top panel show the three displacements, marked by a dot in the hexagon with the color corresponding to that of the local DOS. (b) The band structure of the sample in (a) with $\mathbf{D} = 0$ [red dot in the inset of (a)]. (c) As in (a) but for $\theta_{12} = 3\theta_0$, $\theta_{23} = -4\theta_0$, and $\theta_0 = 0.4^\circ$. Note the difference in the scales between the plots in (a) and (c). (d) The band structure of the sample in (c) with $\mathbf{D} = 0$. (e) Calculated magic-angle pairs $(\theta_{12}, \theta_{23})$ for twisted trilayer graphene. The red and green colors are for magic angles with red and green displacements illustrated in inset of (a), respectively. The magic-angle pair of (a), corresponding to Ref. [27] is marked by a blue star and that of (c) by a blue triangle. The blue square is the magic angle in twisted bilayer graphene with mirror symmetry [19]. All previous theoretical predictions are recovered by our exact numerics. The horizontal dash dot line indicates the bilayer magic angle θ_{tBG}^M . (f) Magic-angle triplets $(\theta_{12}, \theta_{23}, \theta_{34})$ for stacks of four layers. Different colors are used for clarity.

limit, while the latter limit is more physical. We reiterate that the results here only indicate the inability to express the tTG magic angles solely in terms of some analytic function of the tBG magic angles, necessitating their determination through numerical methods.

These results are readily generalized to multilayers and we conclude that, except at certain exceptional configurations such as AA...A stacked alternating (or equal) angle multilayers, there is in general no analytic relation between the values of magic angles in multilayers and that of the bilayer.

IV. EXACTLY SOLVABLE CASE: EQUAL-TWIST MULTILAYERS WITH $N > 3$

Before proceeding with numerical computation, we first address the aforementioned exactly solvable configurations where a correspondence between trilayer and bilayer magic angles may be established. These may be split into two cases, $\eta = -1$ and $\eta = 1$, both with $\mathbf{D} = 0$. These may also be referred to as the alternating and helical cases. Both cases may be generalized to AA...A aligned stacks of N layers, where each layer is twisted by the same angle, θ , and either alternating or same direction with respect to the previous layer.

Previous work on the alternating trilayer came concurrent with the generalization to N layers [19], while that on the equal sign, equal-magnitude case was initially confined to trilayers [27]. There the authors constructed a three-component spinor in terms of the tBG flat band 2-spinor satisfying the

trilayer flat band equation, thereby relating the helical trilayer graphene magic angle to the tBG magic angle. We therefore focus here on the helical multilayer, generalizing these prior arguments. The magic angles for N layers with equal twist and AA...A stacking are determined by an N -component spinor which is the solution of the N first-order differential equations describing the N -layer flat bands, $\mathcal{D}_N \Psi_N = 0$. As previously mentioned, the bilayer solutions are known [18], $\Psi_2 = \{\psi_{1\mathbf{k}}, \psi_{2\mathbf{k}}\}$, written here in momentum space. The solution found in Ref. [27] describes Ψ_3 in terms of three combinations of products of combinations of these wave functions:

$$\Psi_3 \equiv \begin{bmatrix} c\psi_{1\mathbf{k}_1}\psi_{1\mathbf{k}_2} \\ \frac{1}{\sqrt{2}}(\psi_{1\mathbf{k}_1}\psi_{2\mathbf{k}_2} + \psi_{2\mathbf{k}_1}\psi_{1\mathbf{k}_2}) \\ \psi_{2\mathbf{k}_1}\psi_{2\mathbf{k}_2} \end{bmatrix}. \quad (10)$$

A similar equation can be written for the N -component spinor solution to the N -layer flat band equation:

$$\Psi_N \equiv \begin{bmatrix} c \prod_{i=1}^{i=N} \psi_{1\mathbf{k}_i} \\ \frac{1}{\sqrt{N}} \sum_{j=1}^{j \leq N} \psi_{2\mathbf{k}_j} \prod_{i=1, i \neq j}^{i=N} \psi_{1\mathbf{k}_i} \\ \frac{1}{\sqrt{N(N-1)}} \sum_{j=1, k=1, k \neq j}^{j=N, k=N} \psi_{2\mathbf{k}_j} \psi_{2\mathbf{k}_k} \prod_{i=1, i \neq j, i \neq k}^{i=N} \psi_{1\mathbf{k}_i} \\ \dots \\ \prod_{i=1}^{i=N} \psi_{2\mathbf{k}_i} \end{bmatrix}. \quad (11)$$

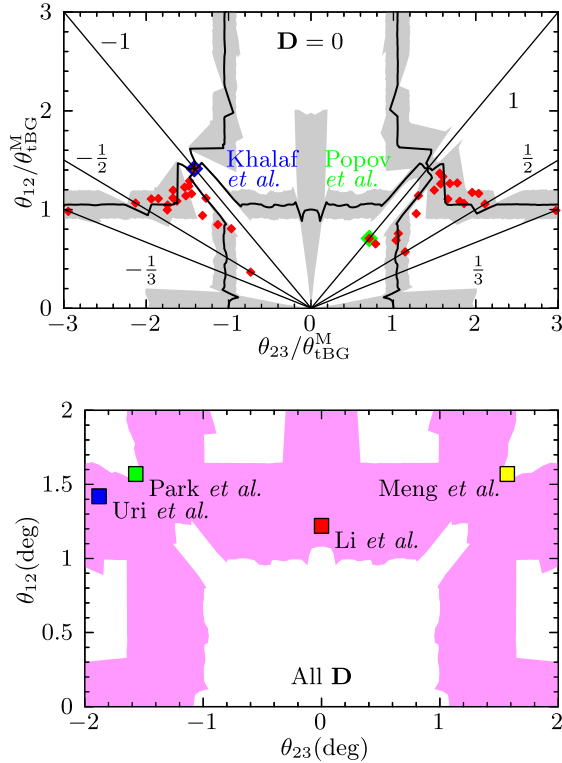


FIG. 3. Magic surface in tTG. Top: The black line indicates predicted magic-angle pairs $(\theta_{12}^M, \theta_{23}^M)$ for $\mathbf{D} = 0$. Shaded gray regions denote the error in the magic-angle pair prediction. Solutions corresponding to our numerical calculations (repeated from Fig. 2) are marked with smaller red diamonds. Only the largest-angles, corresponding to the two solution branches, are shown. The configurations studied in Refs. [19] and [27] are indicated with a large blue and green diamond, respectively, and are recovered by our exact calculations. The discrepancy between the result of Ref. [27] and the predicted line is due to accidental coherence of the typically incoherent, neglected derivative term $S^{-1}(\partial S)$, see text for further discussion. Dotted lines of constant θ_{12}/θ_{23} are marked as guides to the eye. Bottom: Predicted range of magic-angles over all \mathbf{D} . The shaded region indicates pairs of angles for which there exists some \mathbf{D} that would give flat bands. The configurations studied in Refs. [22,26,29,30] are marked in yellow, green, red, and blue, respectively.

We define $\alpha_2 = [v_F(4\pi)/(2d \sin \theta_{tBG}^M/2)]/w$. Then Eq. (11) has a solution for:

$$\alpha_N \equiv \frac{4\pi v_F}{dt_{AB}} \left/ \left[2 \sin \left(\frac{\theta_N^M}{2} \right) \right] \right. = \alpha_2 \left/ \left[\frac{1}{(N-1)!} \right] \right.^{\frac{1}{N-1}}, \quad (12)$$

where θ_N^M is the magic angle of the equal angle twisted multilayer. We have checked that this equation gives the correct solution for $\alpha_3 = \sqrt{2}\alpha_2$ and $\alpha_4 = \sqrt[3]{6}\alpha_2$ agrees with our numerical results for a stack of four layers. Of particular interest is the infinite layer limit,

$$\lim_{N \rightarrow \infty} \theta_N^M = \frac{e}{N-1} \theta_{tBG}^M, \quad (13)$$

where e is Euler's number. This result implies that a small shear force applied to the top and bottom layers of a graphite stack can lead to a peak at the density of states near the Fermi

TABLE I. Magic angles in degrees for selected angle ratios.

(m, n)	$\theta_0^{(0)}$	$\theta_0^{(1)}$	$\theta_0^{(2)}$	$\theta_0^{(3)}$
(3,4)	0.455	0.420	0.400	0.345
(4,7)	0.314	0.307	0.302	0.298
(4,-7)	0.299	0.289	0.284	0.273

level. The results of this section, combined with previous work [19,27], exhaustively detail the configurations for which exact analytical solutions for trilayer magic angles exist in terms of the bilayer solution. The previous section makes clear that further, comprehensive study of the trilayer configuration space will have to involve numerical computation. As a final note, no claims are made regarding a comprehensive search of exact algebraic solutions in $N > 3$ multilayers, and it is possible that special, analytical solutions may be constructed when twist angles are of equal magnitude but the signs of the angles have no particular structure.

V. FLAT BANDS IN THE CHIRAL LIMIT

Having addressed analytically solvable cases, we now analyze Eq. (5) numerically to investigate the existence of flat bands in chiral model trilayers [17,18] for different combinations of twist angles, θ_{12}, θ_{23} and relative displacements between the top and bottom layers. The chiral limit for graphene trilayers with the same twist angle between nearest layers, $\theta_{12} = \theta_{23}$ has been recently explored in Refs. [27,45,47]. The parameters that we use in the following are $\gamma_0 = 2.6$ eV (intralayer nearest-neighbor hopping) and $t_{AB} = 0.0975$ eV (interlayer hopping) [48]. The choice of γ_0 leads to a Fermi velocity $v_F \approx 840$ km/s.

The analytical arguments for the existence of infinitely flat central bands in twisted bilayer graphene [18] is based on the existence of zeros at the corners of the unit cell of a two-component spinor which describes the periodic part of the wave function at the K point of the Brillouin zone. As one of the two components, by symmetry, vanishes at the relevant points, the problem reduces to the tuning of the zeros of a single component. The argument can be generalized to a trilayer, where a three-component spinor is involved. When the Hamiltonian has C_3 symmetry [18] two of the three components of the spinor vanish at the relevant point in the real space unit cell, so that the existence of infinitely flat bands reduces to the existence of a zero in a single component of the spinor. The C_3 symmetry exists at least for a displacement $\mathbf{D} = 0$ and for the displacements which take the trilayer from the AAA to the ABA configuration. An alternative analysis, for the case of a trilayer with $\theta_{12} = \theta_{23}$, can be found in Ref. [27]. We numerically find flat bands, whose width is continuously lowered as the angle is determined with better precision, at several magic angles for all combinations of integers, m, n and displacements, \mathbf{D} , tried. Results are shown in Fig. 2 with selected results in Table I. Interestingly, in some cases we find a quadruplet of bands nearly degenerate at zero energy.

We show in Fig. 2 the local DOS and band structures at the magic angles corresponding to $\{m, n\} = \{1, 1\}$ and $\{m, n\} = \{3, -4\}$ obtained for a displacement between top and bottom

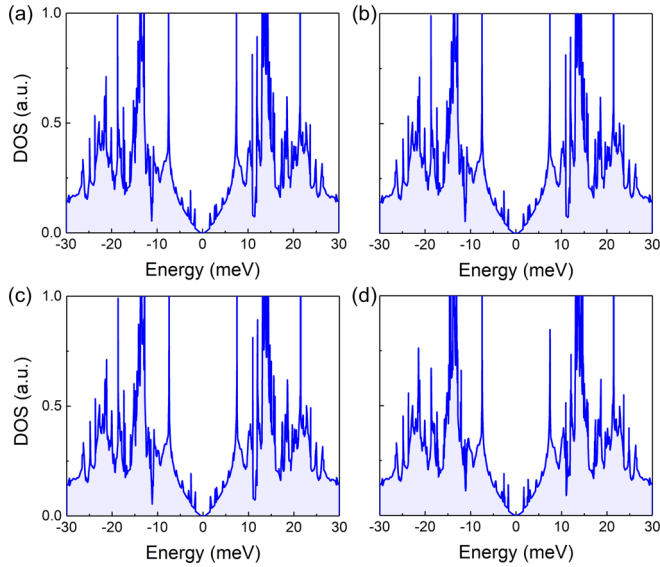


FIG. 4. Local DOS in the chiral limit for the sample in Ref. [30] with angles $\theta_{12} = 3\theta_0$, $\theta_{23} = -4\theta_0$, and $\theta_0 = 0.47^\circ$ and different displacements between the top and bottom layers. The displacements are described by the phases $\{0, 0, 0\}$ (a), $\{0, -\pi/18, \pi/18\}$ (b), and $\{\pi/36, -\pi/18, \pi/36\}$ (c). (d) An average of the three densities of states with the weights $\{1 : 2 : 3\}$, is shown in (d).

layers $\mathbf{D} = 0$. For each magic angle, we plot the DOS for the selected displacement, $\mathbf{D} = 0$, and for two other displacements, shown in the inset in Fig. 2(a). There is a significant dependence of the local DOS on \mathbf{D} in the $\{1, 1\}$ case and a less pronounced dependence in the $\{3, -4\}$ case. This trend towards a weaker dependence on \mathbf{D} with increasing values of the integers $\{m, n\}$ is observed for all combinations explored, see Fig. 4. As expected, for $|\theta_{23}|$ large, $\theta_{12}^M \rightarrow \theta_{\text{tBG}}^M$ as the large twist effectively decouples one layer from the other two.

While an analytical correspondence between the magic angle for a generic tTG configuration and θ_{tBG}^M does not exist, the 3×3 matrix equation which describes the spinor at the magic angles of the chiral bilayer [18,27] can be approximately reduced to an effective bilayer, making significantly easier the calculation of magic angles as a function of commensuration and displacement, as we show in the next section. We note here for completeness that the lack of points between lines of slope -1 and 1 in Fig. 2(e) is a conventional choice, as both lines correspond to symmetry operations on the trilayer stack and respectively mirror inversion about a plane parallel to the layers and rotation by π about any axis parallel to the layers.

The magic angles where flat bands appear depend on the integers m, n , and on the displacement \mathbf{D} . To a first approximation, we can approximate the electronic density of states of the system by an average over the values of \mathbf{D} . This approximation can be expected to become exact in the limit $\ell_{m2}/\ell_m \sim 1/\theta_0 \rightarrow \infty$ and also when the dependence of the band structure on \mathbf{D} is small.

The flat bands at the magic angles reported here show a greater degree of plasmon screening compared to tBG and thus a greater resilience against distortion from interaction effects, see Appendix F. They also have a finite Berry curvature and, typically, nonzero Chern numbers, see Appendix G.

Our analysis can be extended to multilayers with any number of layers greater than three. Results for the density of states in the chiral limit of an helical stack of four layers ($\theta_{12} = \theta_{23} = \theta_{34} = \theta_0$) at different magic angles are shown in Fig. 5, showing clearly the expected peak at zero energy.

VI. FINDING THE MAGIC SURFACE IN TRILAYER CONFIGURATION SPACE

Our numerical calculations have shown that a magic-angle pair may be found seemingly for any numerically accessible (commensurate) twist-angle ratio, and so the natural question would be whether this may be extended to the continuum in angle-pair space. First, we write Eq. (6) more compactly,

$$\mathcal{D}_3(\mathbf{r}, \mathbf{D}, \alpha, \eta) = \mathbb{1}_3 \bar{\partial} + \alpha \mathcal{U}(\mathbf{r}, \mathbf{D}, \eta), \quad (14)$$

where \mathcal{U} is trilayer moiré potential and, without loss of generality, $\eta \geq 1$ is the angle ratio generalizing the commensurate ratio $\frac{m}{n}$ to incommensurate angle pairs.

Previous work [19] found that in the case of alternating, equal-magnitude angles at AAA stacking, $\eta = -1$, $\mathbf{D} = 0$, there exists a similarity transformation of \mathcal{D}_3 that converts it to the form of monolayer-twisted bilayer problem, with an effective moiré potential. The same may be attempted in the more general case of Eq. (14), that is we wish to find a similarity transformation matrix S such that

$$S^{-1} \mathcal{D}_3 S = \mathbb{1}_3 \bar{\partial} + \mathcal{V}, \quad (15)$$

where \mathcal{V} is the effective bilayer moiré potential. This is easily rearranged into the defining equation

$$\bar{\partial} S + \alpha \mathcal{U} S - S \mathcal{V} = 0. \quad (16)$$

Naively, this appears to be at odds with our previous conclusions that tTG does not, in general, have flat bands in correspondence with those of tBG. However, the two nonzero components of \mathcal{V} are generally not simple multiples or scalings of \mathcal{U} , and so the flat band solutions, if they exist, remain independent from the tBG solutions.

The definition for the transformation S given by Eq. (16) is not useful in practice as, for a bilayer moiré potential \mathcal{V} , one column of S is given by the flat band 3-spinor solution of the original flat band equation, $\mathcal{D}_3 \Psi = 0$. Solving for S thus involves solving for the flat band solutions in the first place, defeating the purpose of transforming the moiré potential to bilayer form to extract the magic angles. Instead, we consider an approximate approach by initially neglecting the derivative term and comparing the continuous curve so obtained with the exact calculations at discrete commensurate angle pairs. It is already known that in the alternating angle case, S is a constant in space and so the derivative term $S^{-1}(\bar{\partial} S)$ is identically zero [19]; analysis of the match between the approximate continuous results for general angles and exact discrete results for commensurate angles will tell us whether the initial simplifying assumption is valid.

Neglecting the derivative term amounts to a transformation of the off-diagonal elements of the layer space submatrix, which have the form

$$\mathcal{D}_{\text{off}} = \begin{pmatrix} 0 & a & 0 \\ b & 0 & c \\ 0 & d & 0 \end{pmatrix}_L, \quad \{a, b, c, d\} \in \mathbb{C}. \quad (17)$$

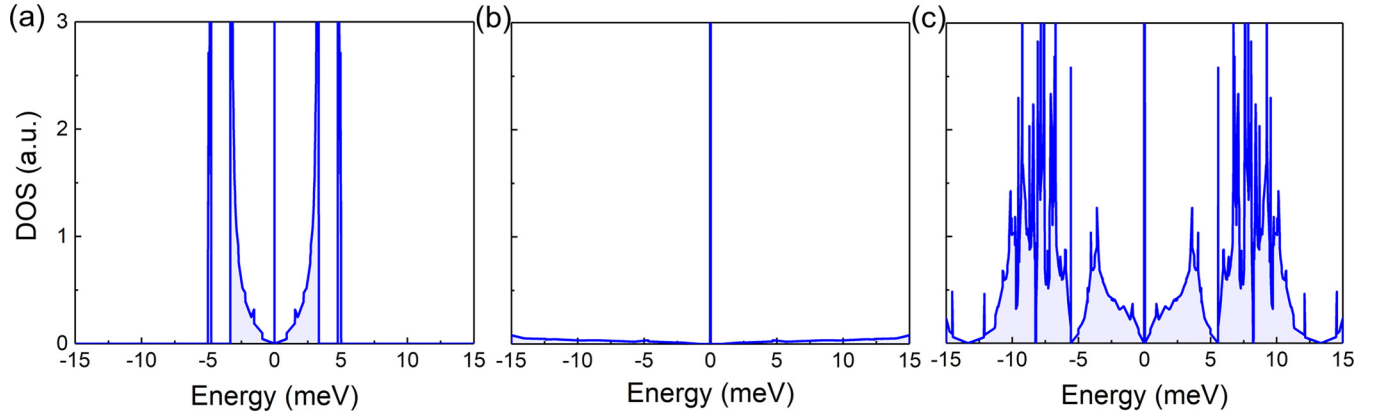


FIG. 5. DOS for magic angles in the chiral limit of four layer stacks with $\theta_{12} = \theta_{23} = \theta_{34} = \theta_0$ (helical arrangement). (a) AAAA stacking, $\theta_0 = 0.55^\circ$. (b) AABB stacking, $\theta_0 = 0.395^\circ$. (c) ABAB stacking, $\theta_0 = 0.299^\circ$.

These may be collected into a single pair of off-diagonal elements through the similarity transformation

$$S^{-1}\mathcal{D}_{\text{off}}S = \begin{pmatrix} 0 & 0 & 0 \\ 0 & 0 & b\sqrt{1 + \frac{cd}{ab}} \\ 0 & a\sqrt{1 + \frac{cd}{ab}} & 0 \end{pmatrix}_{L'} \quad (18)$$

$$S = \frac{1}{\sqrt{2}} \begin{pmatrix} -\frac{c}{b} & 0 & \frac{a}{d} \\ 0 & \frac{a}{d}\sqrt{1 + \frac{cd}{ab}} & 0 \\ 1 & 0 & 1 \end{pmatrix}, \quad (19)$$

where the subscript L' reminds us of the nontrivial mixing of the layers. We are thus able to re-express the interfering double-moiré problem into a single effective moiré potential. We note that the transformation S is not unitary in general and so does not conserve the inner products of spinors but does conserve the band structure. We further note that there is some freedom to choose the form of the single off-diagonal element; our choice most easily connects to previous work [19] where in the case of alternating twist angles, $U_{12}(\mathbf{r}) = U_{23}(-\mathbf{r})$ and so S is unitary and the form factor $\sqrt{1 + \frac{cd}{ab}} = \sqrt{2}$, resulting in a constant scaling of the bilayer moiré potential and thus of the magic angle.

Applying the transformation of Eq. (18) then allows us to obtain a single effective moiré potential, from which an estimate of the magic angle pair may be made by comparison with the bilayer moiré potential, a nontrivial extension of previous work [19] which focused on the special case of alternating twist-angle multilayers.

Our estimate for the magic angle and the error of our estimate is calculated from the average and standard deviation of the form factor $\sqrt{1 + \frac{cd}{ab}}$ over space. While the form of the effective moiré potential we have chosen does indeed have singularities, e.g., at the origin, these diverge as $\frac{1}{x+iy}$ and so the integral over the plane converges, which is unsurprising as it is possible to choose a form of effective moiré potential with no singularities at all, though in that case the analogy to tBG is weaker.

Results for zero shift, $\mathbf{D} = 0$, are shown in the upper panel of Fig. 3 where we indicate with a black line the predicted magic-angle pairs according to the average-value analysis de-

scribed above, with the uncertainty in the prediction shown by the shaded gray region. The alternating twist case previously studied [19] is marked with a blue diamond, and we repeat that this is the only point where the analysis is exact. We mark also our relevant numerically calculated magic-angle pairs, repeated from Fig. 2, with red diamonds, and note the excellent agreement with the more general analysis, verifying that the simplifying assumption taken is valid and giving us confidence that the results are reliable even for the numerically inaccessible case of incommensurate angles. A notable exception is the equal-magnitude helical twist case [27], marked in green, which is especially far from the predicted point. Analysis of the derivative term $S^{-1}\bar{\partial}S$ reveals that the nonzero components are generally incoherent among themselves and with the components of \mathcal{U} , leading to a vanishing effect on the effective moiré potential \mathcal{V} and good agreement with the exact approach. However, when $\theta_{12} = \theta_{23}$ and $\mathbf{D} = 0$ all components of $S^{-1}\bar{\partial}S$ become scalar multiples of the same periodic function, strongly affecting the eigenfunctions of \mathcal{V} and resulting in the visible discrepancy between approaches at this specific angle ratio. Our exact calculations, detailed in the previous section and corresponding to solutions of Eq. (16), recover both the alternating and helical predictions [19,27], indicated by the red diamonds overlapping the blue and green diamonds.

Our analysis predicts two branches of magic-angle pairs from which an infinite set descends, as in the bilayer case [18]. At most two sets of numerically calculated magic angles per angle ratio are shown to connect with the two branches, though other values have been found. We note that the approximate analysis recovers the expected results of the aforementioned limits for (1) one angle vanishing and (2) one angle very large, where in both cases flat bands are expected when the other angle is close to the tBG magic angle.

We repeat the calculation over all moiré shifts to obtain a range of magic-angle pairs, shown in the lower panel of Fig. 3. The magic angles vary continuously with shift and so the manifold of magic configurations is a three-dimensional surface within the four-dimensional trilayer configuration space of two angles and a two-dimensional relative shift. This surface divides the configuration space into unconnected sectors, as seen in the lower panel of Fig. 3 where it is not possible to move from $\theta_{12} = \theta_{23} = 0$

to $\theta_{12} = \theta_{23} = 2^\circ$ without passing through the magic surface. We remind the reader here that the plot is symmetric about the origin. This may have consequences on the topology of the bands as a function of trilayer configuration, as magic configurations may arise as the “midpoints” of band crossings, with the flat bands flattened by repulsion of the crossing bands. Previous work on alternating-twist magic-angle trilayer graphene [22], with trilayer configuration ($\theta_{12} = 1.57^\circ, \theta_{23} = -1.57^\circ, \mathbf{D} = 0$), a twisted monolayer-AA-bilayer system [29], configuration ($\theta_{12} = 1.22^\circ, \theta_{23} = 0, \mathbf{D} = 0$), and a moiré quasiperiodic crystal [30], with configuration ($\theta_{12} = 1.41^\circ, \theta_{23} = -1.88^\circ, \mathbf{D}$ unknown), may be placed as single points within this extended magic phase.

Our method predicts similar magic surfaces corresponding to each of the higher-order (smaller-magnitude) magic angles of tBG. Each branch of the surface begets an infinite series of magic angles, maintaining the proportion set by the set of magic angles for tBG. These corroborate previous findings in the alternating and helical cases [19,27]. However, the error in the angles predicted by our method is absolute rather than relative, and constant for all orders of magic angle. There is therefore much less precision for these higher-order, lower-magnitude magic surfaces.

The method may be extended to systems of N layers by decomposing into either $N/2$ uncoupled bilayers, for N even, or $(N - 1)/2$ uncoupled bilayers with one uncoupled monolayer, for N odd. This produces $\lfloor N/2 \rfloor$ form factors, with $\lfloor \dots \rfloor$ the floor function, that may each generate two branches of solutions, from which an infinite set of magic angles may descend, except at symmetric points where the branches coincide.

Finally, we briefly discuss failure conditions. The method would be considered to have failed if it had generated results generally incompatible with our exact calculations, if the form factor had such severe fluctuations that the standard deviation was of the order or larger than the mean value, or if the predicted angle pairs were well beyond the validity of the small-angle approximation $\sin \theta \approx \theta$. Figure 3 clearly indicates that, in general, this has not happened, giving us confidence in the existence of an extended magic surface.

VII. ANALYSIS OF THE TRILAYER STUDIED IN REF. [30]

We now analyze the experimental situation reported in Ref. [30]. The trilayer studied there shows angles $\theta_{12} \approx 1.42^\circ, \theta_{23} \approx -1.88^\circ$, which are well approximated by $\theta_{12} = 3\theta_0$ and $\theta_{23} = -4\theta_0$ with $\theta_0 \approx 0.47^\circ$. Results for local and average densities of states in the chiral limit are shown in Fig. 4 (we use $\{t_{AA}, t_{AB}\} = \{0.0797, 0.0975\}$ eV, and $\gamma_0 = 3.06$ eV, which implies $v_F \approx 987$ Km/s, in order to compare with Ref. [30]). As shown in the figure, the dependence of the density of states on the displacement \mathbf{D} is very weak, which suggests that the weighted average shown in Fig. 4(d) gives a good approximation to the exact value.

Figure 6(a) is the tight-binding (TB) density of states for trilayer with $\theta_{12} \approx 1.42^\circ, \theta_{23} \approx -1.88^\circ$. We use $\gamma_0 = 3.1$ eV and $\gamma_1 = 0.43$ eV [49–51], the same as Ref. [30] (details in the TB method in Appendix D). The discrepancy between the TB and chiral limit results is due to the difference of the Fermi velocity. Moreover, if we reduce the Fermi velocity, then a flat band appears in the charge neutrality point (not

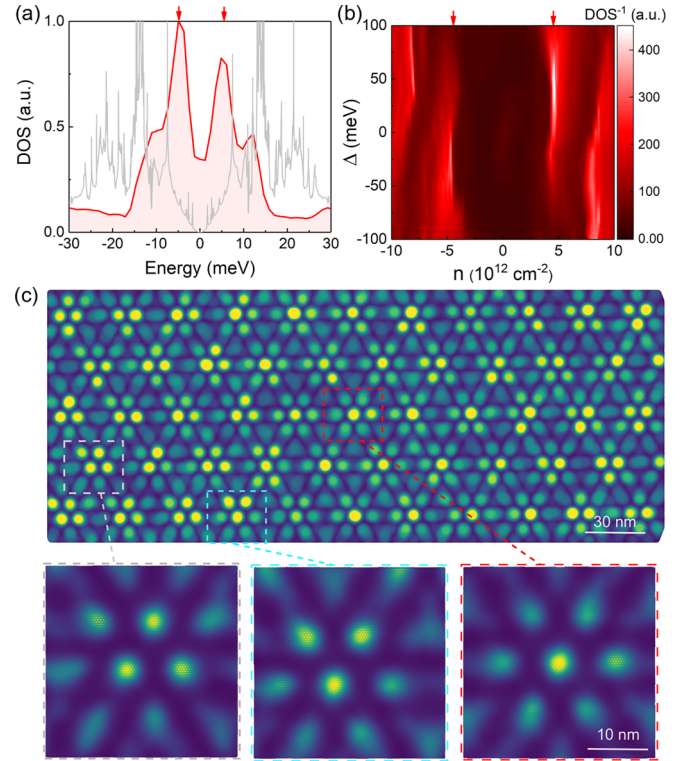


FIG. 6. The tight-binding results of the sample in Ref. [30]. (a) The density of states for a trilayer with angles $\theta_{12} = 1.41^\circ, \theta_{23} = -1.88^\circ$. The gray line is the result in the chiral limit. (b) Tight-binding calculation of the inverse of total DOS versus the carrier density n and electric field potential Δ . Vanishing of the peaks with Δ is due to depletion of carriers from terminal layers, and thus effective removal of one moiré potential. Our results match quantitatively with Ref. [30]. (c) The local density of states at energy of 7 meV in the real space for trilayer in (a), with a zoom in of the states with displacements \mathbf{D} marked by dashed square with colors. Red and gray correspond to the color in Fig. 2(a), and blue are in the middle region.

shown here). The electric field effect is shown in Fig. 6(b). Due to the mirror asymmetry, the system shows a strongly asymmetric response with respect to positive and negative electric field. By applying a perpendicular electric field along the z axis, corresponding to a positive electric potential Δ , we deplete layer 3 and tune carrier density n to recover the resistive state, corresponding to a peak in the inverse of the DOS, for the moiré pattern with θ_{12} . This peak is located at $n = 4.7 \times 10^{12} \text{ cm}^{-2}$. Inversely, a negative Δ decouples layer 1 and recover a resistance state of θ_{23} . Moreover, the states of the peak at 7 meV in Fig. 6(a) is highly localized with an independence of the displacement \mathbf{D} , shown in Fig. 6(c), in agreement with the results in Fig. 4 in the chiral limit.

We extend our discussion to another configuration, the helical trilayer graphene with $\theta_{12} = \theta_{23} = \theta_0$. One magic angle is $\theta_0 = 2^\circ$ [26], which has a peak located at the charge neutrality point of the DOS, shown in Fig. 14. If we consider the lattice relaxation [52–54], then the magic angle reduces to 1.57° . For AAA helical trilayer graphene with identical twist angles, the moiré-of-moiré structure locally relaxes into large areas that contains only one moiré pattern. That is, a large region of the periodic ABA could be reconstructed if a strong intralayer and

interlayer potential is utilized. The states of the flat band in the relaxed system is highly dependent on the displacement \mathbf{D} , which is consistent with the results in Fig. 2(a). Furthermore, the helical trilayer graphene with $\theta_{12} = \theta_{23}$ could be an ideal platform for realization of the chiral limit due to significant corrugation, or via heterostrain engineering [45].

VIII. CONCLUSIONS

We have considered the existence of flat bands in twisted stacks of graphene layers where the twist angles do not allow for the definition of a simple moiré structure, generalizing previous works [19,27,41,42,44–47] which have focused on special configurations yielding exact or approximate moiré structures in trilayers. Analysis of the flat band equations shows that, except at these special configurations, magic tTG solutions cannot be expressed in terms of those of tBG, necessitating numerical computation. By analyzing the chiral limit [17,18] we conclusively demonstrate that flat bands appear in all twist angle ratios where the angles are close to multiples of coprime integers.

Our further extension to generic, incommensurate angles connects the previously disparate magic points of specific trilayer configurations into an extended magic line which, in general, is unrelated to θ_{tBG}^M . Building on the local approximation of Ref. [44] for the specific case of helical trilayers with nearly equal twist angles, we accurately describe the electronic structure of generic twisted multilayers even away from the magic angle, with our results consistent with both large-scale tight-binding calculations [26] and contemporary experiments [30]. The analysis presented here opens the way to the study of topological features in many types of twisted multilayers, and they suggest that the rich phase diagram found in twisted bilayer graphene may exist in many other graphene stacks.

Note added. We have noticed Ref. [55], posted a day before our paper. This reference discusses topics related to our work. Regarding the two-paper overlap, the results are in agreement.

ACKNOWLEDGMENTS

We are thankful to B. Amorim, B. A. Bernevig, E. Castro, I. Yudhistira, and G. Vignale for helpful discussions. IMDEA Nanociencia acknowledges support from the ‘‘Severo Ochoa’’ Programme for Centres of Excellence in R&D (CEX2020-001039-S/AEI/10.13039/501100011033). F.G. acknowledges funding from the European Commission, within the Graphene Flagship, Core 3, Grant No 881603, and from Grants NMat2D (Comunidad de Madrid, Spain) and SprQuMat (Ministerio de Ciencia e Innovación, Spain) and financial support through the (MAD2D-CM)-MRR MATERIALES AVANZADOS-IMDEA-NC. D.C.W.F., M.A., L.P., and S.A. acknowledge support from the Singapore National Research Foundation Investigator Award (NRF-NRFI06-2020-0003). Z.Z. acknowledges support funding from the European Union’s Horizon 2020 research and innovation programme under the Marie Skłodowska-Curie Grant No. 101034431. Numerical calculations presented in this paper have been performed on the supercomputing system in the Supercomputing Center of Wuhan University.

APPENDIX A: DEFINITION OF PERIODICITIES

For completeness, we specify the two relevant periodicities in a twisted graphene trilayer with almost commensurate twist angles, θ_{12} and θ_{23} following the steps described in Ref. [44]. We write the two angles as:

$$\theta_{12} = m\theta_0 + m\delta\theta \quad \theta_{23} = n\theta_0 - n\delta\theta, \quad (\text{A1})$$

where m, n are coprime integers, and we assume that $\theta_0 \ll 1$ and $\delta\theta \ll \theta_0$. The angles θ_{12} and θ_{23} define moiré structures. The vectors connecting the points \mathbf{K} and \mathbf{K}' of the respective Brillouin zones are as follows:

$$\begin{aligned} \Delta\mathbf{K}_{12} &\approx \frac{4\pi}{3d} \left\{ -\frac{m^2(\theta_0^2 + 2\theta_0\delta\theta)}{2}, m\theta_0 + m\delta\theta \right\} \\ &\approx m\mathbf{g}_0 + m\delta\mathbf{g} \\ \Delta\mathbf{K}_{23} &\approx \frac{4\pi}{3d} \left\{ -\frac{n^2(\theta_0^2 - 2\theta_0\delta\theta)}{2}, n\theta_0 - n\delta\theta \right\} \\ &\approx n\mathbf{g}_0 - n\delta\mathbf{g}, \end{aligned} \quad (\text{A2})$$

where we have assumed that $\theta_0 \ll 1$. We obtain:

$$\begin{aligned} \mathbf{g}_0 &\approx \frac{4\pi}{3d} \left\{ \frac{m+n}{4}\theta_0^2 - \frac{m-n}{2}\theta_0\delta\theta, \theta_0 \right\} \approx \frac{4\pi}{3d} \{0, \theta_0\} \\ \delta\mathbf{g} &\approx \frac{4\pi}{3d} \left\{ -\frac{m-n}{4}\theta_0^2 - \frac{m+n}{2}\theta_0\delta\theta, \delta\theta \right\}. \end{aligned} \quad (\text{A3})$$

Vectors \mathbf{g}_0 and $\delta\mathbf{g}$ and three equivalent vectors rotated by $\pm 120^\circ$ define the relevant periodicities of the trilayer. The two vectors satisfy $|\delta\mathbf{g}| \ll |\mathbf{g}_0|$, so that, in real space, the periodicity associated with $\delta\mathbf{g}$ changes much more slowly than that associated to \mathbf{g}_0 . Locally, \mathbf{g}_0 defines a moiré lattice with unit vector $\ell_m \approx d/\theta_0$, where d is the lattice constant of graphene.

In the following, for simplicity, we assume that $\delta\theta \ll \theta_0^2$, although this assumption is not crucial. Then $\delta\mathbf{g}$ defines a new periodicity, with unit cell rotated 90° with respect to the unit cell defined by \mathbf{g}_0 and a lattice unit of length $\ell_{m2} \approx (4d)/(|m-n|\theta_0^2) \gg \ell_m$. Note, finally, that our definition of $\delta\mathbf{g}$, for $m \neq 1$ or $n \neq 1$, differs from the one used in Ref. [44], although both definitions scale as $|\delta\mathbf{g}| \propto \theta_0^2$.

The analysis described above can be extended to an arbitrary number, N , of layers, and N_1 twist angles between nearest layers, provided that these angles are almost commensurate, defined by $N-1$ coprime integers. Such a calculation leads to a periodicity, \mathbf{g}_0 , defined by an angle θ_0 , and $N-2$ additional periodicities defined by vectors $\delta\mathbf{g}_{i=1,\dots,N-2}$ such that $|\delta\mathbf{g}_i| \ll |\mathbf{g}_0|$. Insofar as the role of $\delta\mathbf{g}$ can be reduced to an overall displacement between the layers (see below) the two definitions should give the same results.

APPENDIX B: SLOW PERIODICITY AS A DISPLACEMENT BETWEEN LAYERS

We now elaborate on the argument that the slow periodicity, $\delta\mathbf{g}$, identified in the previous section can be interpreted as a local displacement of the top layer with respect to the bottom layer [44].

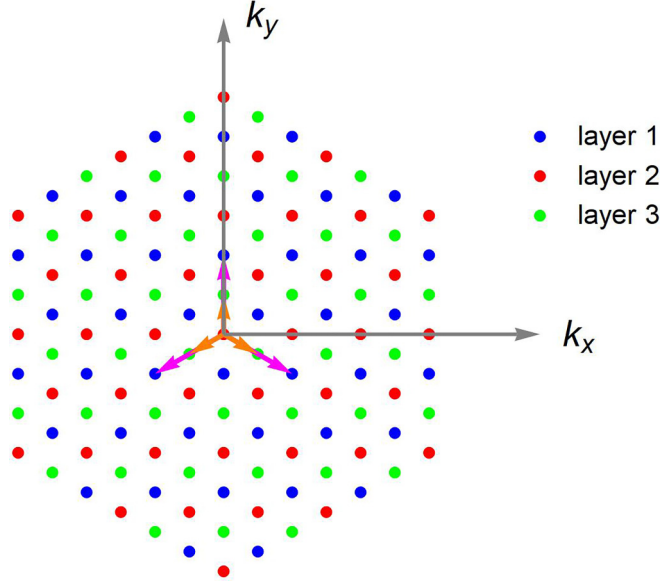


FIG. 7. Sketch of the momenta of the Bloch waves included in the continuum model, see Eq. (B1), for $m = 2, n = 1$. The magenta arrows represent the vectors $m\mathbf{g}_j$, and the orange arrows represent the vectors $n\mathbf{g}_j$, see Eq. (B3).

The interlayer tunneling part of the continuum Hamiltonian [1,2], in real space, is

$$\begin{aligned}\mathcal{H}_T &= \mathcal{H}_T^{12} + \mathcal{H}_T^{23} \\ \mathcal{H}_T^{12} &= \sum_{j=1,2,3} T_j e^{im\mathbf{g}_j \cdot \mathbf{r}} \\ \mathcal{H}_T^{23} &= \sum_{j=1,2,3} T_j e^{in\mathbf{g}_j \cdot \mathbf{r}},\end{aligned}\quad (\text{B1})$$

where T_j define inter-sub-lattice 2×2 matrices:

$$T_j \equiv \begin{bmatrix} t_{AA} & t_{AB} e^{i\frac{2\pi(j-1)}{3}} \\ t_{AB} e^{-i\frac{2\pi(j-1)}{3}} & t_{AA} \end{bmatrix}, \quad (\text{B2})$$

and

$$\begin{aligned}\mathbf{g}_1 &= \frac{\ell_m}{\sqrt{3}} \{0, 1\} \\ \mathbf{g}_2 &= \frac{\ell_m}{\sqrt{3}} \left\{ \frac{\sqrt{3}}{2}, -\frac{1}{2} \right\} \\ \mathbf{g}_3 &= \frac{\ell_m}{\sqrt{3}} \left\{ -\frac{\sqrt{3}}{2}, -\frac{1}{2} \right\}.\end{aligned}\quad (\text{B3})$$

The momenta of the Bloch waves used in the calculation are shown in Fig. 7.

We can generalize the tunneling Hamiltonian to the case where the moiré pattern of layers 1 and 2 is displaced by a shift \mathbf{D}_1 and the moiré pattern between layers 2 and 3 is displaced by a shift \mathbf{D}_3 [40]. In the initial Hamiltonian, the rotation is around a point with AA stacking between layers 1 and 2 and AA stacking between layers 2 and 3, that is, AAA stacking. The

shifts lead to the Hamiltonian:

$$\begin{aligned}\mathcal{H}_T &= \mathcal{H}_T^{12} + \mathcal{H}_T^{23} \\ \mathcal{H}_T^{12} &= \sum_{j=1,2,3} T_j e^{im\mathbf{g}_j \cdot (\mathbf{r} - \mathbf{D}_1)} \\ \mathcal{H}_T^{23} &= \sum_{j=1,2,3} T_j e^{in\mathbf{g}_j \cdot (\mathbf{r} - \mathbf{D}_3)}.\end{aligned}\quad (\text{B4})$$

Each Bloch wave in the calculation, see Fig. 7, can be modified by a gauge factor, $e^{i\mathbf{G} \cdot \mathbf{D}'}$, where \mathbf{G} is the momentum of the wave. This gauge transformation induces a phase in the interlayer tunnelings, which is equivalent to a redefinition of the shifts:

$$\begin{aligned}\mathbf{D}'_1 &= \mathbf{D}_1 - \mathbf{D}' \\ \mathbf{D}'_3 &= \mathbf{D}_3 - \mathbf{D}'.\end{aligned}\quad (\text{B5})$$

This result is independent of the integers m and n and of the angle θ_0 . An equal shift, $\mathbf{D}_1 = \mathbf{D}_3$, of the two moiré patterns can be gauged away. This implies that the calculated electronic structure is only dependent on the value of $\mathbf{D}_1 - \mathbf{D}_3 = \mathbf{D}$.

The two periodicities defined by \mathbf{g}_0 and $\delta\mathbf{g}$ in the previous section modify the continuum Hamiltonian, Eq. (B1), leading to:

$$\begin{aligned}\mathcal{H}_T^{12} &= \sum_{j=1,2,3} T_j e^{im\mathbf{g}_0 \cdot \mathbf{r}} e^{im\delta\mathbf{g}_j \cdot \mathbf{r}} \\ \mathcal{H}_T^{23} &= \sum_{j=1,2,3} T_j e^{in\mathbf{g}_0 \cdot \mathbf{r}} e^{-in\delta\mathbf{g}_j \cdot \mathbf{r}}.\end{aligned}\quad (\text{B6})$$

The vectors $\delta\mathbf{g}_j$ define a periodicity with unit vectors in real space:

$$\{\mathbf{D}_1, \mathbf{D}_3\} = \frac{2\pi}{3d|\delta\mathbf{g}_i|} \{\mathbf{R}_1, \mathbf{R}_2\} \approx \frac{1}{\theta_0^2} \{\mathbf{R}_1, \mathbf{R}_2\}, \quad (\text{B7})$$

where \mathbf{R}_1 and \mathbf{R}_2 are the lattice vectors of an untwisted graphene layer.

We now assume that the arguments $\delta\mathbf{g}_j \cdot \mathbf{r}$ vary slowly with respect the functions $\mathbf{g}_0 \cdot \mathbf{r}$ and assume that the value of $\mathbf{r} = \mathbf{D}$ in $\delta\mathbf{g}_j \cdot \mathbf{r}$ is constant. Then, using Eq. (B4), we obtain that the local Hamiltonian is equivalent to displacements of the top and bottom layers by $\pm(d/\ell_{m2})R_{\pi/2}(\mathbf{D})$, where R_θ is a rotation operator.

For $m \neq 1$ or $n \neq 1$ the loops in momentum space which connect a momentum in the central layer to itself through a path which visits both the top and bottom layers require at least $m \times n$ steps. The increased periodicity of these loops for $m \neq 1$ or $n \neq 1$ imply that the band structure in real space repeats itself for a displacement periodicity defined by the unit vectors:

$$\{\tilde{\mathbf{D}}_1, \tilde{\mathbf{D}}_3\} = \frac{1}{mn} \{\mathbf{D}_1, \mathbf{D}_3\}.\quad (\text{B8})$$

This result implies that the actual periodicity in real space is given by $\ell_{m2}/(mn)$. A sketch of the different regions in the unit cell, and the points where the band structure repeats itself is shown in Fig. 8.

DOS for two choices of the magic angle in the chiral limit, and $\{m, n\} = \{2, 1\}$ are shown in Fig. 9. Similar results for $\{m, n\} = \{3, 2\}$ are shown in Fig. 10.

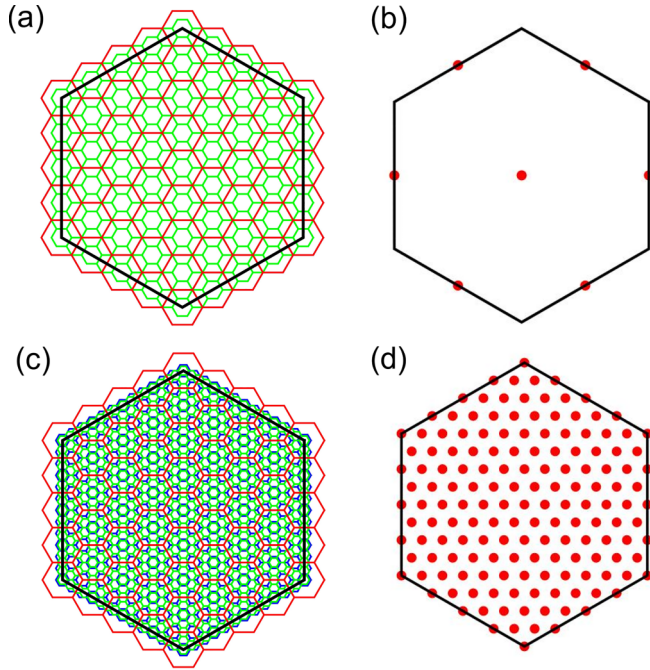


FIG. 8. Sketch of the real space unit cell structure for (a) bilayer with $\{m, n\} = \{1, 2\}$ and (c) trilayer with $\{m, n\} = \{3, -4\}$. The black hexagon defines the large unit cell, associated with moiré length l_{m2} . The red hexagons show the moiré structure associated with angle θ_0 and moiré length l_m . Blue and green hexagons show moirés associated with angles θ_{12} and θ_{23} . Note that the moiré lattices associated to θ_0 and θ_{12} coincide. Special points in the momentum space unit cell with the AAA electronic structure for (b) $\{m, n\} = \{1, 2\}$ and (d) $\{m, n\} = \{3, -4\}$ cases.

APPENDIX C: VALIDITY OF THE LOCAL HAMILTONIAN EXPANSION

The moiré-of-moiré length scale emerges due to the misalignment of the moiré patterns between layers 1 and 2, and layers 2 and 3, $(\theta_{12} + \theta_{23})/2$, as shown in the Fig. 1(c) of the main text. Starting from a particular momentum point in the second layer, we may reach other points in the second layer by hopping through either the first or third layer. Hoppings between only two of the layers allow us to define a momentum space moiré lattice, a subset of which are shown as red points along the black lines. The dotted line marks the closest approach between middle layer states connected by hoppings that only pass through either the first or third layer, which defines the moiré-of-moiré modulation length scale. The sketch specifically shows the situation for $m, n = 3, 4, \theta_0 = 1^\circ$.

The distance between a momentum state reached by a hops through the first layer and another state reached by b hops through the third layer is $\sqrt{3}k_D P_{ab}$, where

$$\begin{aligned} P_{ab}^2 &= (a\theta_{12})^2 + (b\theta_{23})^2 - 2ab|\theta_{12}\theta_{23}|\cos\left(\frac{\theta_{12} + \theta_{23}}{2}\right) \\ &\approx (a|\theta_{12}| - b|\theta_{23}|)^2 + ab|\theta_{12}\theta_{23}|\left(\frac{\theta_{12} + \theta_{23}}{2}\right)^2 \\ &\rightarrow (am - b|n|)^2\theta_0^2 + abm|n|\left(\frac{m+n}{2}\right)^2\theta_0^4, \end{aligned} \quad (\text{C1})$$

and we take the small-angle approximation in the second line and commensurate angles ($m \geq 0$ WLOG) in the third line. The moiré-of-moiré length scale is then $l_{m2} = 2\pi/\sqrt{3}k_D \min(P_{ab})$, where we minimize P_{ab} over all integers $a \geq 0$ and $b \geq 0$, except for the trivial solution $P_{00} = 0$. For small commensurate angles with m and n small, this generally occurs at $P_{|n|m} = \frac{|mn(m+n)|}{2}\theta_0^2$; however, if m and n are large and of the same sign, then P_{ab} may be minimized at some other $a \neq |n|, b \neq m$. For example, at $\theta_{12} = 1.0^\circ, \theta_{23} = 0.9^\circ, P_{1,1} < P_{9,10}$. For completeness, we note that this description only considers lattice points lying on the two lines as shown in the sketch, when in fact there are others in the two-dimensional plane. Provided the angles and thus the misalignment is small, the points on these lines remain the closest to each other.

Numerically calculated results for l_{m2} are shown in the Fig. 1(d) of the main text. As expected, l_{m2} diverges along the line $\theta_{12} = -\theta_{23}$, and is generally larger for θ_{23}/θ_{12} negative than for θ_{23}/θ_{12} positive due to the reduced misalignment of the moiré patterns. l_{m2} is also particularly pronounced at commensurate angles with simple ratios, where it is easy to minimize the first term of Eq. (C1) without the second term getting too large. For experimental samples smaller than l_{m2} , a particular local Hamiltonian expansion is expected to be a good description of the bands while for samples much larger than l_{m2} , it is necessary to average over expansion centers or, equivalently, over $\mathbf{D}_1 - \mathbf{D}_3$. We note that the form for l_{m2} derived and calculated here agrees with that previously derived [44] for the special case of $\theta_{23}/\theta_{12} \approx 1$.

Neglecting the slow periodicity in the local expansion, as is done in the numerical calculations of us and Ref. [44], neglects the misalignment and so forces the black lines of the upper panel sketch to coincide. In the case of commensurate angles, this leads to $\min(P_{ab}) = 0$ and thus l_{m2} diverging, leading us to ignore the modulation of $\mathbf{D}_1 - \mathbf{D}_3$.

APPENDIX D: TIGHT-BINDING RESULTS

We use a round disk method to construct the twisted graphene trilayers with arbitrary twist angles. The two independent twist angles θ_{12} and θ_{23} are chosen to be the rotation of the second layer relative to the first layer and the rotation of the third layer relative to the second layer, respectively. The rotation origin is chosen at an atom site. We use a twist angle pair $(\theta_{12}, \theta_{23})$ as the notation for different twist-angle configurations. Positive (negative) values of the twist angle denotes counterclockwise (clockwise) rotations. The sample with $(-\theta, \theta)$ has a mirror symmetry with the middle layer as the mirror plane. To calculate the property of these large-scale systems with arbitrary twist angles, we construct the system in a large round disk. The radius of the disk should be set sufficiently large to rid the effects of edge states [50]. In the actual calculation, the disk with radius of 172.2 nm ($700d$ being d the lattice constant of graphene) and contains 10 million carbon atoms are utilized for the twist angles investigated in this work. Figure 11 shows the $(21.8^\circ, 21.8^\circ)$ configuration of twisted trilayer graphene with AAA stacking.

A parameterized full TB model is used. In the tight-binding model, only p_z orbitals are taken into account, we construct

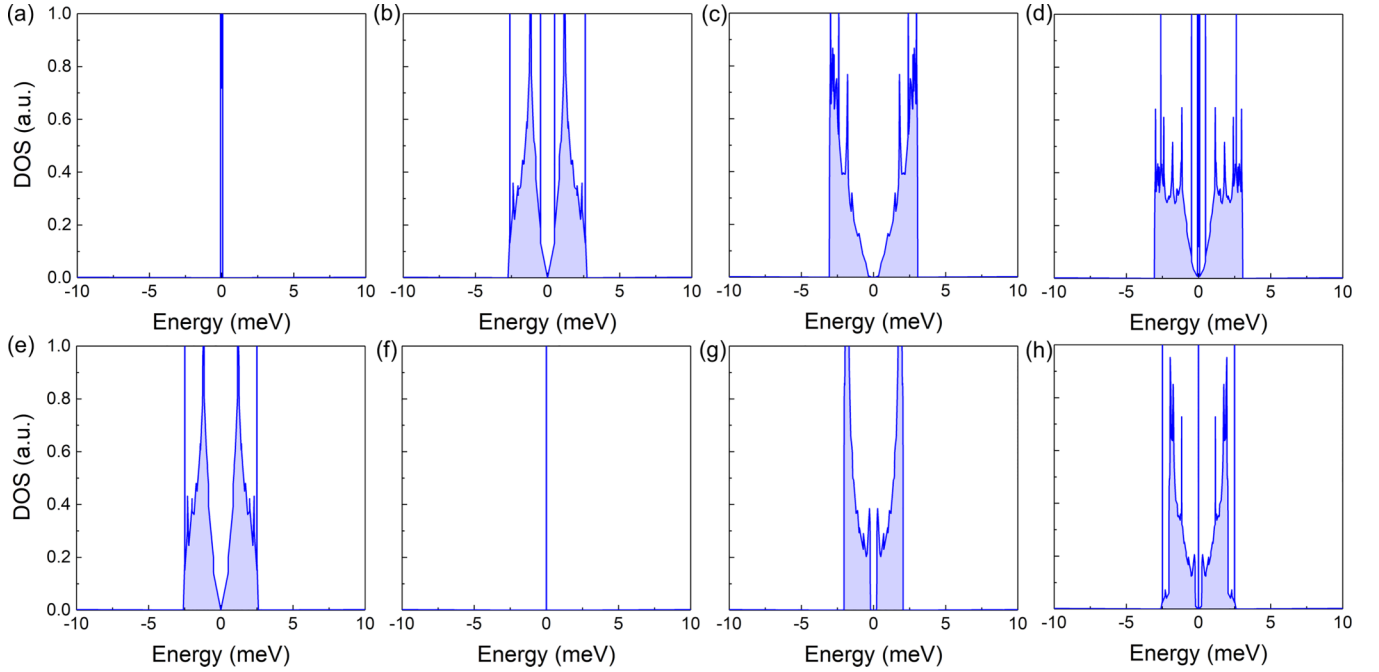


FIG. 9. Results for the magic angles in the chiral limit and $\theta_{12} = 2\theta_0$, $\theta_{23} = \theta_0$. [(a)–(d)] The local DOS for a magic angle $\theta_0 = 1.163^\circ$ with three displacements and their average, as in Fig. 4 of the main text. [(e)–(h)] As in the top panel but for a magic angle $\theta_0 = 1.14^\circ$.

the Hamiltonian of the twisted graphene trilayers as

$$H = \sum_i \epsilon_i |i\rangle\langle i| + \sum_{\langle i,j \rangle} t_{ij} |i\rangle\langle j|, \quad (\text{D1})$$

where $|i\rangle$ is the p_z orbital located at \mathbf{r}_i , and $\langle i, j \rangle$ is the sum over index i and j with $i \neq j$, and ϵ_i is the onsite potential term. According to the Slater-Koster formalism, the hopping integral t_{ij} , interaction between two p_z orbitals located at \mathbf{r}_i

and \mathbf{r}_j has the form [51]

$$t_{ij} = n^2 V_{pp\sigma}(r_{ij}) + (1 - n^2) V_{pp\pi}(r_{ij}), \quad (\text{D2})$$

where $r_{ij} = |\mathbf{r}_j - \mathbf{r}_i|$ is the distance between i and j sites, with n as the direction cosine along the direction \mathbf{e}_z perpendicular to the graphene layer. The Slater and Koster parameters $V_{pp\pi}$

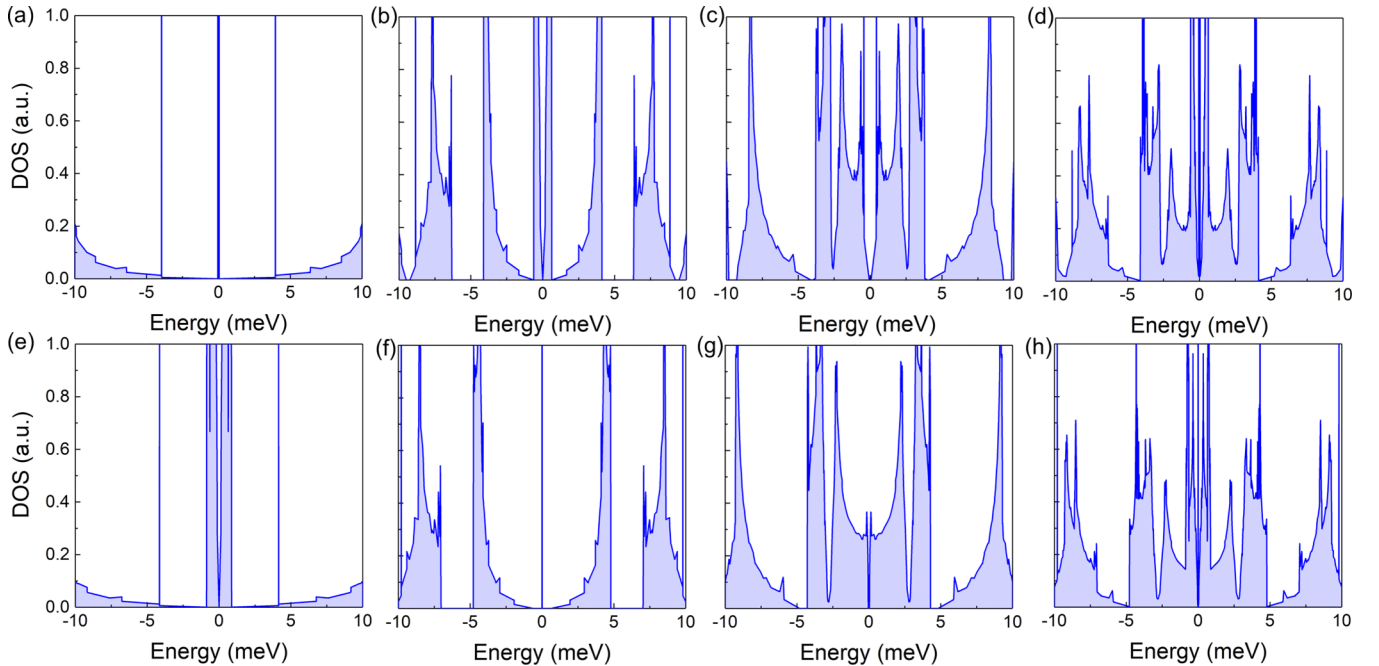


FIG. 10. As in Fig. 9 but for $\theta_{12} = 3\theta_0$, $\theta_{23} = 2\theta_0$. [(a)–(d)] The local DOS for a magic angle $\theta_0 = 0.6^\circ$ with three displacements and their average as in Fig. 5 of the main text. [(e)–(h)] Results for a magic angle $\theta_0 = 0.59^\circ$.

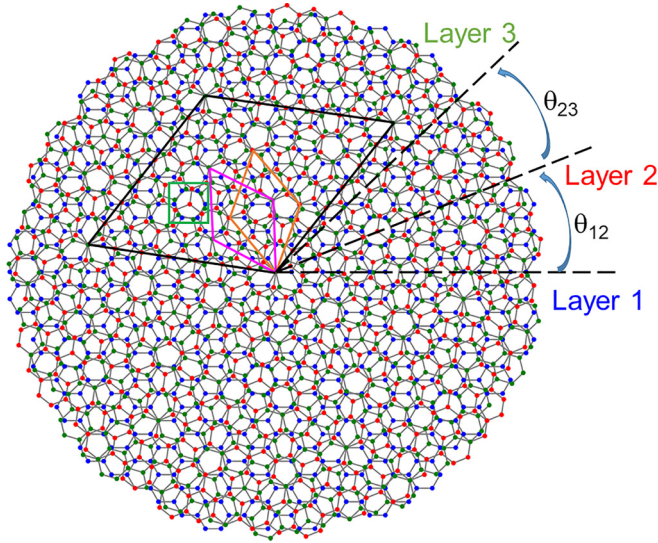


FIG. 11. Schematic of the AAA trilayer graphene with $\theta_{12} = \theta_{23} = \theta_0 = 21.8^\circ$. The θ_{12} and θ_{23} are the twist angles between layer 1 and layer 2 and then layer 2 and layer 3, respectively. The orange and purple rhombi are the moiré unit cells with θ_{12} and θ_{23} , respectively, which has length $\ell_m = 0.65$ nm. The black rhombus is the unit cell of the moiré-of-moiré with $\ell_{m2} = 1.7$ nm. The green square shows an ABA stacking region.

and $V_{pp\sigma}$ follow

$$\begin{aligned} V_{pp\pi}(r_{ij}) &= -t_0 e^{q_\pi(1-r_{ij}/a)} F_c(r_{ij}), \\ V_{pp\sigma}(r_{ij}) &= t_1 e^{q_\sigma(1-r_{ij}/h)} F_c(r_{ij}), \end{aligned} \quad (\text{D3})$$

where $a = 1.42$ Å and $h = 3.349$ Å are the nearest in-plane and out-of-plane carbon-carbon distance, respectively, $t_0 = 3.1$ eV and $t_1 = 0.43$ eV are the TB hopping parameters taken from the moiré quasiperiodic crystal paper [30]. The parameters q_σ and q_π satisfy $\frac{q_\sigma}{h} = \frac{q_\pi}{a} = 2.218$ Å⁻¹, and the smooth function is $F_c(r) = (1 + e^{(r-r_c)/l_c})^{-1}$, in which l_c and r_c are chosen as 0.265 and 5.0 Å, respectively. In the twisted graphene trilayer calculations, we only consider the interlayer hoppings between adjacent layers. An open boundary condition is used in the disk model. The electronic properties of the twisted graphene trilayer with arbitrary angles (θ_{12}, θ_{23}) are calculated by the tight-binding propagation method implemented in the TBPLaS simulator [49]. For example, the detailed formula of the density of states is

$$D(\varepsilon) = \frac{1}{2\pi S} \sum_{p=1}^S \int_{-\infty}^{\infty} e^{i\varepsilon t} \langle \varphi_p(0) | e^{-iHt} | \varphi_p(0) \rangle dt, \quad (\text{D4})$$

where $|\varphi_p(0)\rangle$ is one initial state which is the random superposition of all basis states and S is the number of random initial states. The distribution of states in real space can be obtained by calculating the quasieigenstates [49] (a superposition of degenerate eigenstates with certain energy). The quasieigenstates has the expression:

$$|\Psi(\varepsilon)\rangle = \frac{1}{\sqrt{\sum_n |A_n|^2 \delta(\varepsilon - E_n)}} \sum_n A_n \delta(\varepsilon - E_n) |n\rangle, \quad (\text{D5})$$

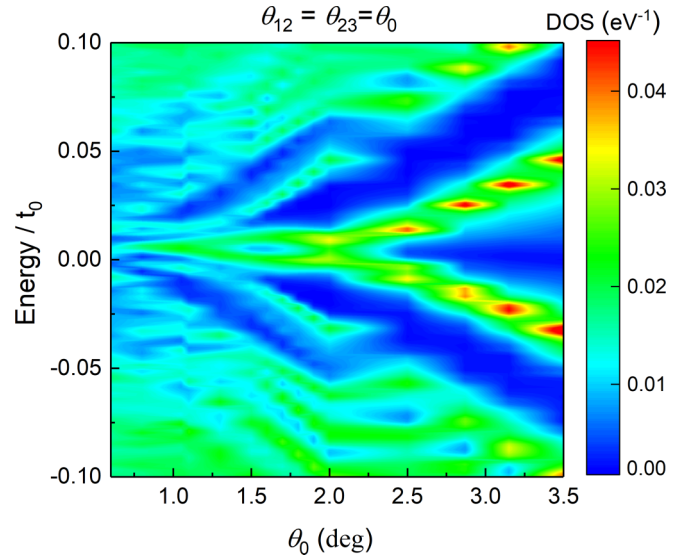


FIG. 12. The TB DOS of AAB trilayer graphene with twist angles $\theta_{12} = \theta_{23} = \theta_0$. The hopping parameters are $t_0 = 2.8$ eV and $t_1 = 0.44$ eV. The displacement \mathbf{D} is zero.

where A_n are random complex numbers with $\sum_n |A_n|^2 = 1$, E_n is the eigenvalue, and $|n\rangle$ is the corresponding eigenstate. The local density of states mapping calculated from the quasieigenstates is highly consistent with the experimentally scanning tunneling microscopy dI/dV mapping. We also consider the lattice relaxation effect on the electronic properties of twisted trilayer graphene. In the round disk sample, the edge carbon atoms possessing dangling bond are passivated by placing in-plane hydrogen atoms to saturate the dangling σ edge bonds. The carbon-hydrogen bond length is assumed to be 0.1 nm. We employ the classical molecular dynamics simulation package LAMMPS to do the full (both in-plane and out-of-plane) lattice relaxation [52]. The intralayer C-C and C-H interactions and interlayer C-C interactions are simulated with REBO [53] and kolmogorov/crespi/z version of Kolmogorov-Crespi (KC) [54] potentials, respectively. To take into account the effect of the electric field, we shift the electric potential of the outer layers by $\pm\Delta$. That is, without electric field, the onsite term ϵ_i in Eq. (D1) is zero for the three layers. Once a perpendicular electric field is applied, as shown in the inset of Fig. 6(b), the $-\Delta$ and Δ terms are added to the ϵ_i of layer 1 and layer 3, respectively.

We focus on the helical twisted trilayer graphene configuration. First, we consider the particular case that the two twist angles are equal. In the TB calculation, we set $t_0 = 2.8$ eV and $t_1 = 0.44$ eV, which give a magic angle of 1.05° in the tBG case. The evolution of the density of states with twist angles of AAB twisted trilayer graphene is shown in Fig. 12. Note the discontinuity of the van Hove singularity (VHS) evolves with the twist angle is due to the low resolution of the twist angle, which will not change our conclusion. The system can be considered as a AAA trilayer with a displacement of the carbon-carbon distance a between the top and bottom layers. The tendency is similar to the AAA trilayer graphene case [26,43]. That is, with θ_0 decreases, the van Hove singularity gap (the energy difference between the first van Hove

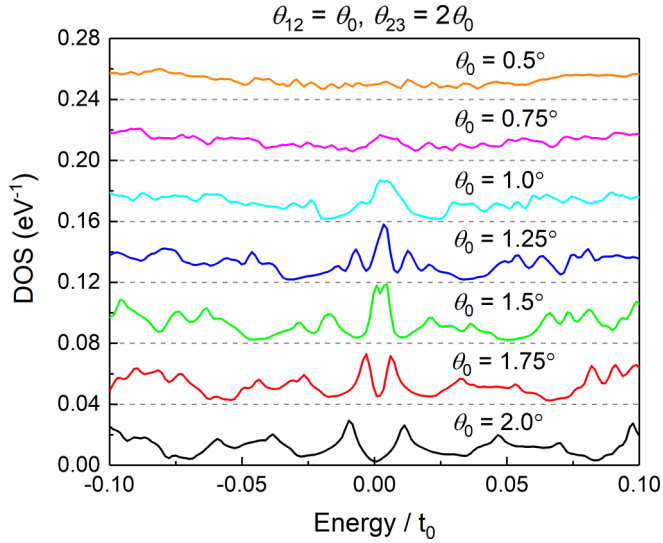


FIG. 13. The TB DOS of AAB trilayer graphene with θ_0 where twist angles $\theta_{12} = \theta_0$, $\theta_{23} = 2\theta_0$. The hopping parameters are $t_0 = 2.8$ eV and $t_1 = 0.44$ eV. The displacement \mathbf{D} is zero. Curves are vertically shifted for clarity.

singularity on the valence and conduction bands) narrows and reaches minimum value at around 2° . This result is reasonable since the moiré unit cell with periodicity ℓ_{m2} contains all the configurations, for instance, the AAA and ABA stackings. In this case, the first “magic angle” is 2° . The VHSs merge again at the angle $\theta_0 = 1^\circ$. In the magic angle of trilayer in chiral limit in Fig. 5 of the main text, there is a magic angle at $\theta_0 = 0.72^\circ$. In the case of $\theta_{12} = \theta_0$, $\theta_{23} = 2\theta_0$, shown in Fig. 13, the first magic angle is $\theta_0 = 1.25^\circ$, which is consistent with the result in the continuum limit in Ref. [43].

As discussed in the Ref. [26], in the case of AAA twisted trilayer graphene with $\theta_{12} = \theta_{23}$, the first magic angle decreases from 2° to 1.57° when the lattice relaxation is considered. A sharp peak is located at the charge neutrality point, shown in Fig. 14. The states of the peak in the real space are different for different displacement \mathbf{D} are different, which is in agreement with the result in Fig. 2(a) of the main text. Such state feature can be detected by the scanning tunneling microscopy in experiment. However, for the relaxation of the system with the REBO and KC potentials, we could not find a strong reconstruction of the structure with the ABA region relax to large area and clear domain wall region, which may achieve via a stronger intralayer and interlayer potential [45].

We extend our discussion to another configuration, the trilayer graphene with $\theta_{12} = 1.42^\circ$ and $\theta_{23} = -1.88^\circ$, which was realized recently [30]. The electric field effect is shown in Fig. 15. Due to the unequal twist angles θ_{12} and θ_{23} , the system shows strong asymmetry with respect to the electric field. By applying a perpendicular electric field with the direction point to the z axis, that is, the positive electric potential Δ , we deplete the layer 3 and tune carrier density n to recover the resistive state (corresponds to a peak in the inverse of the DOS) for the moiré pattern with θ_{12} . Such peak is located at $n = 4.7 \times 10^{12} \text{ cm}^{-2}$. The results in Fig. 15 is highly consistent with the results in Ref. [30]. In the next section, we discuss further results pertinent to this experimentally realized

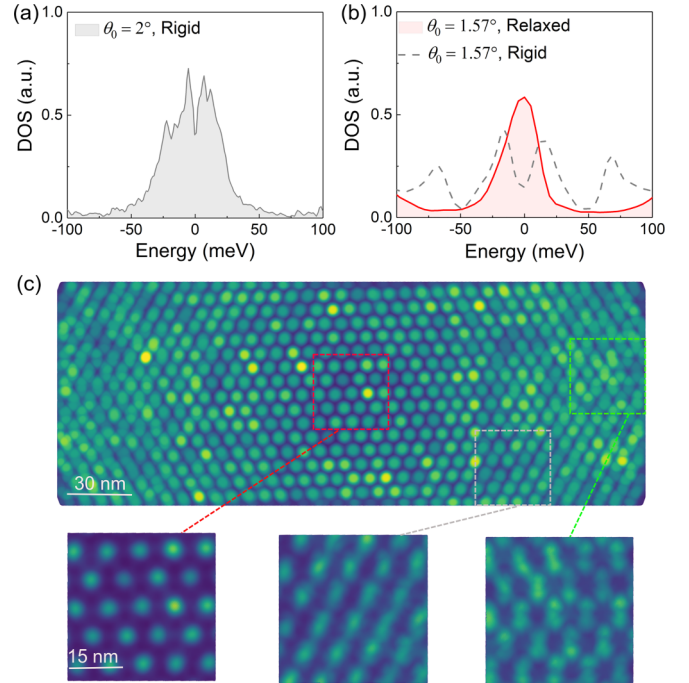


FIG. 14. The lattice relaxation effect of the helical structure. (a) The TB DOS of AAA rigid trilayer graphene with magic twist pair $\theta_{12} = \theta_{23} = \theta_0 = 2^\circ$. (b) The TB DOS of AAA with magic angle $\theta_0 = 1.57^\circ$. (c) The local DOS at zero energy in real space with a zoom-in of the states at different displacement \mathbf{D} of sample in (b). The colors of the squares correspond to the ones in Fig. 2(a). The hopping parameters are $t_0 = 3.2$ eV and $t_1 = 0.48$ eV.

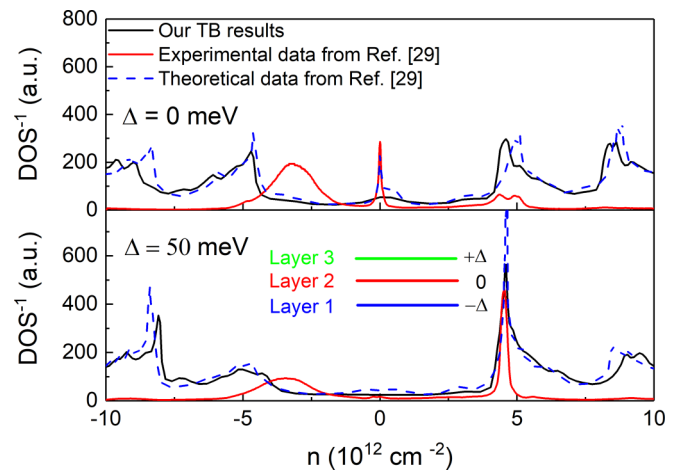


FIG. 15. The electric field effect. The inverse of the DOS of AAA trilayer graphene with magic twist pair $\theta_{12} = 1.42^\circ$ and $\theta_{23} = -1.88^\circ$ without electric potential (top panel) and under a positive electric potential (bottom panel). The solid black line shows our theoretical tight binding calculation, while the dashed blue line shows the calculation from Ref. [30]. The solid red line shows the resistance as measured in Ref. [30]. Resistance peaks are qualitatively explained by gaps in the band structure and corresponding peaks in the inverse DOS, with quantitative mismatch due to neglecting interaction and relaxation effects.

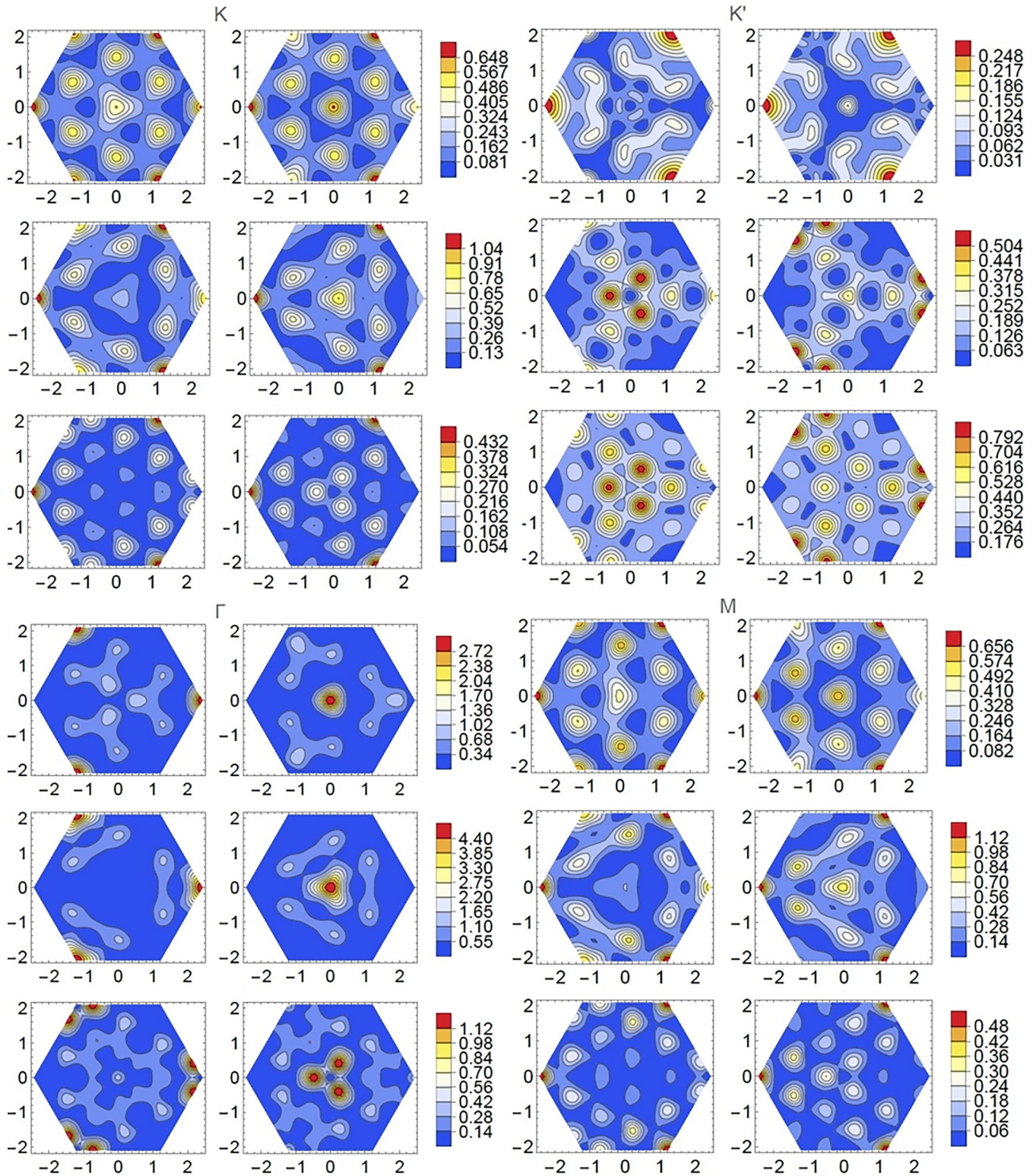


FIG. 16. Charge density at high-symmetry points, K , K' , Γ , and M , of the two lowest bands of the continuum model for a trilayer with the rotations reported in Ref. [30]. There are six plots for each point in the Brillouin zone. The two columns represent the two sublattices, A and B , and the three rows represent the three layers. The central layer is shown in the central row. The horizontal and vertical axes denote the position in real space normalized by the moiré periodicity of θ_{23} . The parameters used are the same as in Fig. 4.

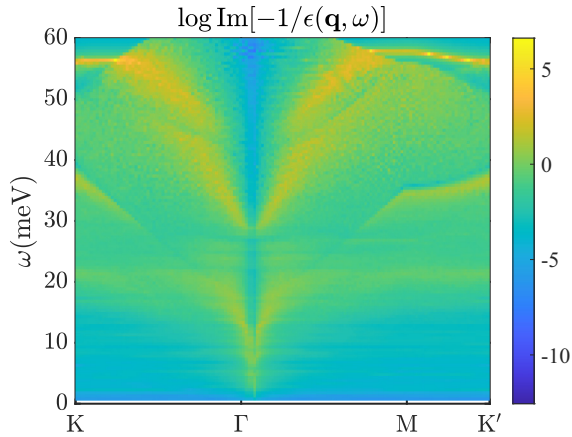


FIG. 17. Two-dimensional plot of the energy loss function along a high-symmetry path in the moiré Brillouin zone. Multiple branches of plasmon can be observed, corresponding to both intra- and intercollective excitation processes. The data in this figure are based on $\theta_{12} = 1.42^\circ$ and $\theta_{23} = -1.88^\circ$ at the charge neutral point with background dielectric constant $\epsilon = 4$.

trilayer configuration that may be obtained from the continuum model.

APPENDIX E: FURTHER COMPARISON WITH REF. [30]

The analytical methods we have used in this paper allow us to investigate experimental observables beyond those reported by Ref. [30]. For example, we may calculate the charge density, as shown in Fig. 16, measured at the high-symmetry points of the reduced moiré Brillouin zone and resolved by layer (rows) and valley (columns). The angle mismatch causes the K and K' points to be unequal, resulting in different charge distributions.

We have also calculated the electron loss function for this trilayer configuration, as shown in Fig. 17. The loss function provides information about Landau damping and interband

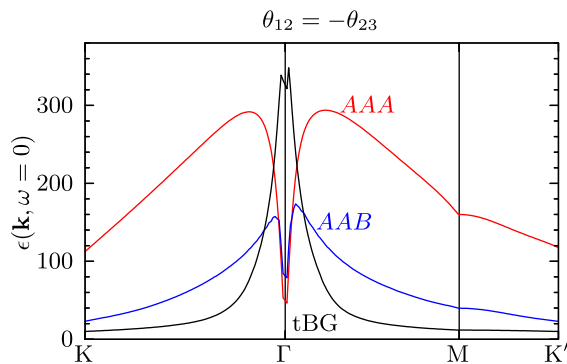


FIG. 18. Static component of the dielectric function, $\epsilon(\mathbf{k}, \omega = 0)$, evaluated over the Brillouin zone for alternating-twist magic-angle trilayer graphene at AAA (red) and AAB (blue) stacking compared to that of magic-angle tBG (black). The value of ϵ for trilayers is greatly increased compared to that of tBG everywhere except the Γ point, indicating an overall greater degree of plasmon screening in trilayers and thus greater robustness of the calculated noninteracting band structures to Hartree effects.

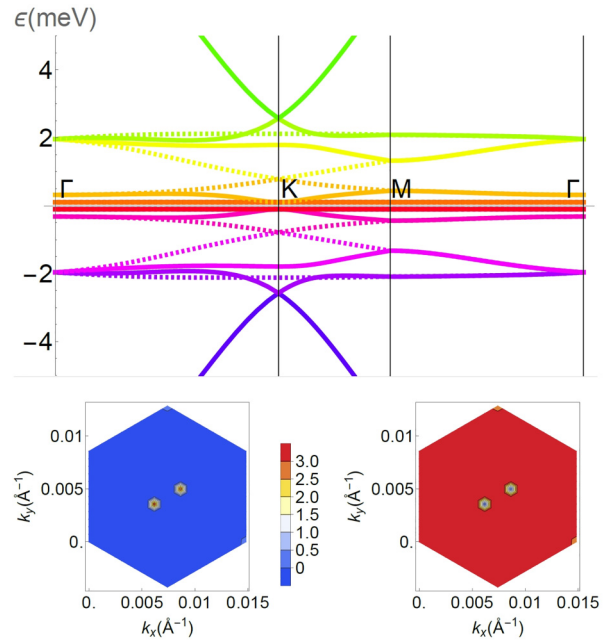


FIG. 19. Top panel: Low-energy electronic bands for an ABA trilayer with $\{m, n\} = \{3, -4\}$ and $\{\theta_{12}, \theta_{23}\} = \{0.85^\circ, -1.14^\circ\}$. Using the parameters described in the main text, two flat bands are obtained at charge neutrality point. Bottom panel: Berry curvature normalized to $2\pi C$ when integrated over the Brillouin zone, where $C = \{2, -1\}$ is the Chern number of each band.

transition processes, which can be directly measured through experimental techniques such as electron-energy-loss spectroscopy [56]. To our knowledge, this loss function has not yet been experimentally measured. Our trilayer model predicts multiple branches of plasmon modes, corresponding to both

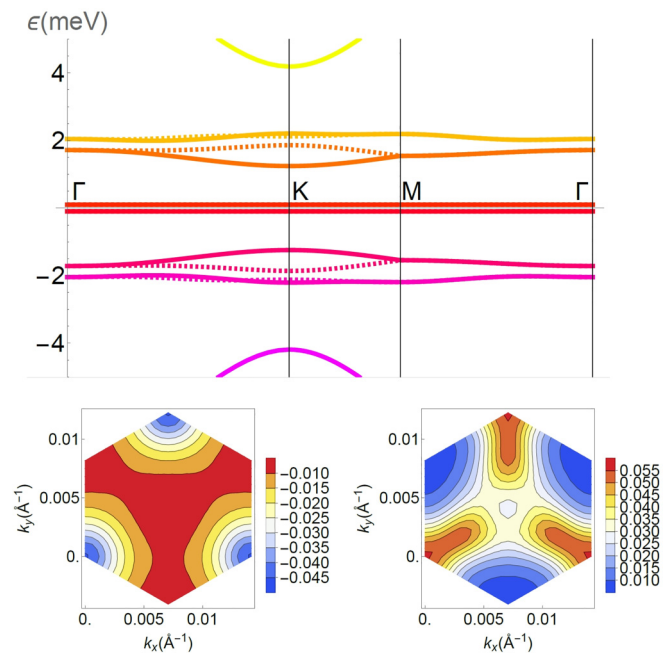


FIG. 20. As in Fig. 19 but for $\{m, n\} = \{2, -3\}$ and $\{\theta_{12}, \theta_{23}\} = \{0.54^\circ, -0.81^\circ\}$. The Chern numbers are $C = \{1, -2\}$.

intra- and intercollective excitation processes, which can be further validated through experimental measurements.

APPENDIX F: DIELECTRIC SCREENING IN TRILAYERS

It has been widely shown that the dielectric response for multi-twisted materials increases drastically as the bands become flat [57]. The plasmon screening on electron-electron interaction is believed to have a significant effect on the strong correlation phenomena. One potential advantage of magic multilayers over tBG is that the calculated noninteracting band structures are expected to be more resilient against Hartree effects due to the higher dielectric function from plasmon screening.

We may verify this by calculating the static component of the dielectric function. For simplicity, we ignore Umklapp processes, which would give a matrix structure to the polarization, with entries labeled by moiré reciprocal lattice vectors, \mathbf{G}, \mathbf{G}' . Within the framework of random-phase approximation, the dynamic dielectric function can be calculated via

$$\epsilon(\mathbf{k}, \omega) = 1 - V(\mathbf{k})\Pi(\mathbf{k}, \omega), \quad (\text{F1})$$

where $V(\mathbf{k}) = 2\pi e^2/\kappa k$ is the Fourier component of the two-dimensional Coulomb interaction, with κ being the background dielectric constant. We choose $\kappa = 4$ in our calculation, in effect assuming the substrate is hBN. $\Pi(\mathbf{k}, \omega)$ is the dynamic polarization function given by

$$\Pi(\mathbf{k}, \omega) = 2 \sum_{\mathbf{q}, \xi} \sum_{m, n} \frac{(f_{\mathbf{q}+\mathbf{k}, \xi}^n - f_{\mathbf{q}, \xi}^m) F_{\mathbf{q}, \mathbf{q}+\mathbf{k}, \xi}^{nm}}{E_{\mathbf{q}+\mathbf{k}, \xi}^n - E_{\mathbf{q}, \xi}^m - \omega - i0}, \quad (\text{F2})$$

where m, n are the band index, ξ is the valley index, $f_{\mathbf{q}}^m$ is the Fermi-Dirac distribution, and $F_{\mathbf{q}, \mathbf{q}+\mathbf{k}, \xi}^{nm} = |\psi_{n, \mathbf{q}+\mathbf{k}, \xi}^\dagger \psi_{m, \mathbf{q}, \xi}|^2$ is the form factor of two different Bloch states.

Results are shown in Fig. 18, which shows $\epsilon(\mathbf{k}, \omega = 0)$ over the moiré Brillouin zone for alternating-twist magic-angle trilayer graphene in the AAA and AAB configurations and for tBG. We choose to compare with alternating twist trilayers to remove moiré-of-moiré effects and to be able to make direct comparisons between the Brillouin zones of the two materials. The value of ϵ is seen to be \mathbf{D} dependent, as expected from the \mathbf{D} dependence of the band structure, and is noticeably higher than that of tBG everywhere except at Γ , indicating that there is a greater degree of plasmon screening in the trilayer, as expected, and that the calculated noninteracting bands are therefore expected to be more robust against Coulomb interaction effects than those of tBG.

APPENDIX G: ELECTRONIC BANDS AND BERRY CURVATURE

The flat electronic bands at magic angles studied in the main text show finite Berry curvatures, and, generally, nonzero Chern numbers, see also Refs. [45,47]. Examples are given in Figs. 19 and 20. In both cases we observe a numerically flat band at charge neutrality. Unlike in the alternating twist case [19,20], the flat band appears isolated as the differing twist angles causes the Dirac cones of all three layers to be distributed at different points in space, leading to hybridization and band repulsion. The calculated Chern numbers are also seen to depend on twist angle. As the angles chosen do not correspond to the same magic surface, these results suggest that the magic surfaces may divide the configuration space into separate topological sectors, with different bands mixing at each surface and altering the Chern numbers.

-
- [1] J. M. B. Lopes dos Santos, N. M. R. Peres, and A. H. Castro Neto, Graphene bilayer with a twist: Electronic structure, *Phys. Rev. Lett.* **99**, 256802 (2007).
 - [2] R. Bistritzer and A. H. MacDonald, Moiré bands in twisted double-layer graphene, *Proc. Natl. Acad. Sci. USA* **108**, 12233 (2011).
 - [3] E. Y. Andrei and A. H. MacDonald, Graphene bilayers with a twist, *Nat. Mater.* **19**, 1265 (2020).
 - [4] L. Balents, C. R. Dean, D. K. Efetov, and A. F. Young, Superconductivity and strong correlations in moiré flat bands, *Nat. Phys.* **16**, 725 (2020).
 - [5] G. Chen and J. L. Lado, Tunable moire spinons in magnetically encapsulated twisted van der Waals quantum spin liquids, *Phys. Rev. Res.* **3**, 033276 (2021).
 - [6] L. Zhang, F. Wu, S. Hou, Z. Zhang, Y.-H. Chou, K. Watanabe, T. Taniguchi, S. R. Forrest, and H. Deng, Van der Waals heterostructure polaritons with moiré-induced nonlinearity, *Nature (Lond.)* **591**, 61 (2021).
 - [7] M. Khosravian and J. L. Lado, Impurity-induced excitations in a topological two-dimensional ferromagnet/superconductor van der Waals Moiré heterostructure, *Phys. Rev. Mater.* **6**, 094010 (2022).
 - [8] H. D. Scammell and M. S. Scheurer, Tunable superconductivity and Möbius Fermi surfaces in an inversion-symmetric twisted van der Waals heterostructure, *Phys. Rev. Lett.* **130**, 066001 (2023).
 - [9] T. Li, S. Jiang, L. Li, Y. Zhang, K. Kang, J. Zhu, K. Watanabe, T. Taniguchi, D. Chowdhury, L. Fu, J. Shan, and K. F. Mak, Continuous Mott transition in semiconductor moiré superlattices, *Nature (Lond)* **597**, 350 (2021).
 - [10] F. Ferreira, S. Magorrian, V. Enaldiev, D. Ruiz-Tijerina, and V. Fal'ko, Band energy landscapes in twisted homobilayers of transition metal dichalcogenides, *Appl. Phys. Lett.* **118**, 241602 (2021).
 - [11] M. Vogl, S. Chaudhary, and G. A. Fiete, Light driven magnetic transitions in transition metal dichalcogenide heterobilayers, *J. Phys.: Condens. Matter* **35**, 095801 (2023).
 - [12] V. V. Enaldiev, F. Ferreira, J. G. McHugh, and V. I. Fal'ko, Self-organized quantum dots in marginally twisted MoSe₂/WSe₂ and MoS₂/WS₂ bilayers, *npj 2D Mater. Appl.* **6**, 74 (2022).
 - [13] G. Chen, M. Khosravian, J. L. Lado, and A. Ramires, Designing spin-textured flat bands in twisted graphene multilayers via helimagnet encapsulation, *2D Mater.* **9**, 024002 (2022).

- [14] P. Törmä, S. Peotta, and B. A. Bernevig, Superconductivity, superfluidity and quantum geometry in twisted multilayer systems, *Nat. Rev. Phys.* **4**, 528 (2022).
- [15] L. Liu, S. Zhang, Y. Chu, C. Shen, Y. Huang, Y. Yuan, J. Tian, J. Tang, Y. Ji, R. Yang, K. Watanabe, T. Taniguchi, D. Shi, J. Liu, W. Yang, and G. Zhang, Isospin competitions and valley polarized correlated insulators in twisted double bilayer graphene, *Nat. Commun.* **13**, 3292 (2022).
- [16] G. W. Burg, E. Khalaf, Y. Wang, K. Watanabe, T. Taniguchi, and E. Tutuc, Emergence of correlations in alternating twist quadrilayer graphene, *Nat. Mater.* **21**, 884 (2022).
- [17] P. San-Jose, J. González, and F. Guinea, Non-Abelian gauge potentials in graphene bilayers, *Phys. Rev. Lett.* **108**, 216802 (2012).
- [18] G. Tarnopolsky, A. J. Kruchkov, and A. Vishwanath, Origin of magic angles in twisted bilayer graphene, *Phys. Rev. Lett.* **122**, 106405 (2019).
- [19] E. Khalaf, A. J. Kruchkov, G. Tarnopolsky, and A. Vishwanath, Magic angle hierarchy in twisted graphene multilayers, *Phys. Rev. B* **100**, 085109 (2019).
- [20] Y. Cao, J. M. Park, K. Watanabe, T. Taniguchi, and P. Jarillo-Herrero, Pauli limit violation and reentrant superconductivity in magic-angle twisted trilayer graphene, *Nature (Lond.)* **595**, 526 (2021).
- [21] H. Kim, Y. Choi, C. Lewandowski, A. Thomson, Y. Zhang, R. Polski, K. Watanabe, T. Taniguchi, J. Alicea, and S. Nadj-Perge, Evidence for unconventional superconductivity in twisted trilayer graphene, *Nature (Lond.)* **606**, 494 (2022).
- [22] J. M. Park, Y. Cao, L. Xia, S. Sun, K. Watanabe, T. Taniguchi, and P. Jarillo-Herrero, Robust superconductivity in magic-angle multilayer graphene family, *Nat. Mater.* **21**, 877 (2022).
- [23] Y. Sheffer and A. Stern, Chiral magic-angle twisted bilayer graphene in a magnetic field: Landau level correspondence, exact wave functions, and fractional Chern insulators, *Phys. Rev. B* **104**, L121405 (2021).
- [24] A. Eaton, Y. Li, H. A. Fertig, and B. Seradjeh, Renormalized magic angles in asymmetric twisted graphene multilayers, *Phys. Rev. B* **106**, 045117 (2022).
- [25] S. Carr, C. Li, Z. Zhu, E. Kaxiras, S. Sachdev, and A. Kruchkov, Ultraheavy and ultrarelativistic dirac quasiparticles in sandwiched graphenes, *Nano Lett.* **20**, 3030 (2020).
- [26] H. Meng, Z. Zhan, and S. Yuan, Commensurate and incommensurate double moiré interference in twisted trilayer graphene, *Phys. Rev. B* **107**, 035109 (2023).
- [27] F. K. Popov and G. Tarnopolsky, Magic angles in equal-twist trilayer graphene, [arXiv:2303.15505](https://arxiv.org/abs/2303.15505).
- [28] N. Morales-Durán, J. Wang, G. R. Schleder, M. Angeli, Z. Zhu, E. Kaxiras, C. Repellin, and J. Cano, Pressure-enhanced fractional Chern insulators along a magic line in moiré transition metal dichalcogenides, *Phys. Rev. Res.* **5**, L032022 (2023).
- [29] Y. Li, A. Eaton, H. A. Fertig, and B. Seradjeh, Dirac magic and Lifshitz transitions in AA-stacked twisted multilayer graphene, *Phys. Rev. Lett.* **128**, 026404 (2022).
- [30] A. Uri, S. C. de la Barrera, M. T. Randeria, D. Rodan-Legrain, T. Devakul, P. J. D. Crowley, N. Paul, K. Watanabe, T. Taniguchi, R. Lifshitz, L. Fu, R. C. Ashoori, and P. Jarillo-Herrero, Superconductivity and strong interactions in a tunable moiré quasicrystal, *Nature (Lond.)* **620**, 762 (2023).
- [31] T. Cea, P. A. Pantaleón, and F. Guinea, Band structure of twisted bilayer graphene on hexagonal boron nitride, *Phys. Rev. B* **102**, 155136 (2020).
- [32] J. Shi, J. Zhu, and A. H. MacDonald, Moiré commensurability and the quantum anomalous Hall effect in twisted bilayer graphene on hexagonal boron nitride, *Phys. Rev. B* **103**, 075122 (2021).
- [33] D. Mao and T. Senthil, Quasiperiodicity, band topology, and moiré graphene, *Phys. Rev. B* **103**, 115110 (2021).
- [34] H. Oka and M. Koshino, Fractal energy gaps and topological invariants in hBN/graphene/hBN double moiré systems, *Phys. Rev. B* **104**, 035306 (2021).
- [35] J. R. Wallbank, A. A. Patel, M. Mucha-Kruczyński, A. K. Geim, and V. I. Fal'ko, Generic miniband structure of graphene on a hexagonal substrate, *Phys. Rev. B* **87**, 245408 (2013).
- [36] M. M. A. Ezzi, J. Hu, Ariando, F. Guinea, and S. Adam, Topological flat bands in graphene super-moiré lattices, [arXiv:2306.10116](https://arxiv.org/abs/2306.10116).
- [37] M. Koshino, Interlayer interaction in general incommensurate atomic layers, *New J. Phys.* **17**, 015014 (2015).
- [38] B. Amorim and E. V. Castro, Electronic spectral properties of incommensurate twisted trilayer graphene, [arXiv:1807.11909](https://arxiv.org/abs/1807.11909).
- [39] T. Cea, N. R. Walet, and F. Guinea, Twists and the electronic structure of graphitic materials, *Nano Lett.* **19**, 8683 (2019).
- [40] X. Li, F. Wu, and A. H. MacDonald, Electronic structure of single-twist trilayer graphene, [arXiv:1907.12338](https://arxiv.org/abs/1907.12338).
- [41] C. Mora, N. Regnault, and B. A. Bernevig, Flatbands and perfect metal in trilayer moiré graphene, *Phys. Rev. Lett.* **123**, 026402 (2019).
- [42] F. Wu, R.-X. Zhang, and S. Das Sarma, Three-dimensional topological twistrionics, *Phys. Rev. Res.* **2**, 022010(R) (2020).
- [43] Z. Zhu, S. Carr, D. Massatt, M. Luskin, and E. Kaxiras, Twisted trilayer graphene: A precisely tunable platform for correlated electrons, *Phys. Rev. Lett.* **125**, 116404 (2020).
- [44] Y. Mao, D. Guerci, and C. Mora, Supermoiré low-energy effective theory of twisted trilayer graphene, *Phys. Rev. B* **107**, 125423 (2023).
- [45] T. Devakul, P. J. Ledwith, L.-Q. Xia, A. Uri, S. C. de la Barrera, P. Jarillo-Herrero, and L. Fu, Magic-angle helical trilayer graphene, *Sci. Adv.* **9**, eadi6063 (2023).
- [46] N. Nakatsuji, T. Kawakami, and M. Koshino, Multiscale lattice relaxation in general twisted trilayer graphenes, *Phys. Rev. X* **13**, 041007 (2023).
- [47] D. Guerci, Y. Mao, and C. Mora, Chern mosaic and ideal flat bands in equal-twist trilayer graphene, [arXiv:2305.03702](https://arxiv.org/abs/2305.03702) [cond-mat.mes-hall].
- [48] M. Koshino, N. F. Q. Yuan, T. Koretsune, M. Ochi, K. Kuroki, and L. Fu, Maximally localized Wannier orbitals and the extended Hubbard model for twisted bilayer graphene, *Phys. Rev. X* **8**, 031087 (2018).
- [49] Y. Li, Z. Zhan, X. Kuang, Y. Li, and S. Yuan, TBPLaS: A tight-binding package for large-scale simulation, *Comput. Phys. Commun.* **285**, 108632 (2023).
- [50] G. Yu, Z. Wu, Z. Zhan, M. I. Katsnelson, and S. Yuan, Dodecagonal bilayer graphene quasicrystal and its approximants, *npj Comput. Mater.* **5**, 122 (2019).

- [51] J. C. Slater and G. F. Koster, Simplified LCAO method for the periodic potential problem, *Phys. Rev.* **94**, 1498 (1954).
- [52] A. P. Thompson, H. M. Aktulga, R. Berger, D. S. Bolintineanu, W. M. Brown, P. S. Crozier, P. J. in't Veld, A. Kohlmeyer, S. G. Moore, T. D. Nguyen *et al.*, LAMMPS - a flexible simulation tool for particle-based materials modeling at the atomic, meso, and continuum scales, *Comput. Phys. Commun.* **271**, 108171 (2022).
- [53] D. W. Brenner, O. A. Shenderova, J. A. Harrison, S. J. Stuart, B. Ni, and S. B. Sinnott, A second-generation reactive empirical bond order (REBO) potential energy expression for hydrocarbons, *J. Phys.: Condens. Matter* **14**, 783 (2002).
- [54] A. N. Kolmogorov and V. H. Crespi, Registry-dependent inter-layer potential for graphitic systems, *Phys. Rev. B* **71**, 235415 (2005).
- [55] F. K. Popov and G. Tarnopolsky, Magic angle butterfly in twisted trilayer graphene, *Phys. Rev. Res.* **5**, 043079 (2023).
- [56] R. F. Egerton, Electron energy-loss spectroscopy in the TEM, *Rep. Prog. Phys.* **72**, 016502 (2008).
- [57] Z. A. H. Goodwin, F. Corsetti, A. A. Mostofi, and J. Lischner, Attractive electron-electron interactions from internal screening in magic-angle twisted bilayer graphene, *Phys. Rev. B* **100**, 235424 (2019).